2018

CARBON NANOTUBE INTERACTIONS WITH HUMAN CELLS UNDER SHEAR USING MICROFLUIDICS

Rolf Staud

University of Rhode Island, rolf-staud@my.uri.edu

CARBON NANOTUBE INTERACTIONS WITH HUMAN CELLS

UNDER SHEAR USING MICROFLUIDICS

BY

ROLF STAUD

A THESIS SUBMITTED IN PARTIAL FULFILLMENT OF THE

REQUIREMENTS FOR THE DEGREE OF THE

MASTER OF SCIENCE

IN

CHEMICAL ENGINEERING

UNIVERSITY OF RHODE ISLAND

2018

MASTER OF SCIENCE THESIS

OF

ROLF STAUD

APPROVED:

Thesis Committee:

Major Professor   Geoffrey D. Bothun

Co-Major Professor: Daniel Roxbury

                              Samantha Meenach

                              Hongyan Yuan

                              Nasser H. Zawia
                            DEAN OF THE GRADUATE SCHOOL

UNIVERSITY OF RHODE ISLAND

2018

ABSTRACT

In recent years, nanotechnology has attracted significant interest in cancer therapeutics for its touted ability to offer innovative solutions to existing problems associated with chemotherapeutic agents. Specifically, single-walled carbon nanotubes (SWCNTs) have garnered recent attention in the fields of bioimaging and biosensing. SWCNTs possess an intrinsic and unique near-infrared (nIR) photostable fluorescence and biocompatibility. Several past studies have revealed how SWCNTs interact with biological systems *in vitro* and *in vivo*. In this study, the specific effect of flow and shear stress on the interactions between SWCNTs and live cells *in vitro* are more closely investigated. The nature of binding and endocytosis of SWCNTs with adenocarcinomic human alveolar epithelial (A549) cells was explored with intensity-based measurements acquired through the use of nIR fluorescence hyperspectral microscopy. Furthermore, the effect of Fetal Bovine Serum (FBS) in addition to nanoparticles' protein corona under shear stress conditions was examined.

The investigations in this novel study predict, that SWCNTs will internalize more likely into endothelia cells, which are exposed to high shear stress. Despite this, the results concerning the shear stress independently of the SWCNT concentration showed, that the shear stress has only a marginal influence on their adsorption and desorption, compared to the impact that proteins binding to the surface of SWCNTs create.

ACKNOWLEDGMENTS

It is a pleasure for me to thank those who made this thesis and my experience at the University of Rhode Island possible.

I owe my deepest gratitude to my professors Dr. Geoffrey D. Bothun and Dr. Daniel Roxbury. This thesis would not have been accomplished without their great supervision. Especially the inventiveness and farsightedness of Dr. Bothun fascinated me. Also, his skills to design figures from former proposals inspired me. I am as thankful to had have the chance to learn from Dr. Roxbury´s creativity, lab organization and frequently meetings, which helped me a lot to overcome methodical and technical problems. He highly motivated me to incorporate into his research. At this point, I like to thank my thesis committee of Dr. Samantha Meenach, Hongyan Yuan and Jie Shen as defense chair. I am thankful for their excellent scientific support and advice during my research at the URI.

In this context, I also want to express my gratitude to the research assistants Megan McSweeney and Matthew Simmeth, who supported me greatly in the Roxbury lab and helped me by giving feedback i.e. in the phase of methodical development. Particularly, I want to thank the PhD students Mitch Gravely and Moohammad Moein Safaee, who also helped me as pleasant colleagues along in the lab. Additionally, I also want to thank Timo Küster, Jessica Orr, Nasim Ganji, Animesh Pan and John Nunes from the Bothun lab group for their manifold support and inspiration.

Furthermore, I would like to thank the Chemical Engineering Faculty and Staff, especially Brenda Moyer and Deborah Brielmaier, who helped me with orders and formalities.

On the German site of the dual degree program, I want to thank Dr. Dietzel and Eugen Koch from the Institute of Microtechnology (IMT), who kindly expressed their willingness to supervise me for the graduation in Brunswick.

Finally, I would like to thank my parents Ekhard and Petra Staud, who made my educational path with this particular graduation possible.

TABLE OF CONTENTS

LIST OF TABLES

LIST OF FIGURES

CHAPTER 1:   INTRODUCTION

Understanding the cellular internalization of nanoparticles is a central problem to many emerging applications of biological nanotechnology [1] including drug delivery systems, biosensing and imaging.

Almost always, drug molecules have to enter cells and overcoming the barrier of passing the cell membrane via passive and untargeted diffusion in order to their desired effect. This common drug delivery pathway via blood vessels limits cancer therapy approaches through inhomogeneous drug transport and nonuniform drug delivery. Hence, to overcome these various transport barriers, there is an urgent need of utilizing molecular and nanotechnology applications to deliver the drugs or in terms of biosensing to transport nanoparticles to specific targets in the human body [2].

With the intention of using nanoparticles as vehicles in target drug delivery or to transmit information for imaging purposes, the particles have to adsorb and enter the targeted tissue differently, caused by their size. In addition to that, nanoparticles interact with serum proteins, which bind to the surface (opsonization). This complicates the adsorption and internalization process (endocytosis) and constitutes another challenge. The possibility to modify and functionalize the surface makes single-walled carbon nanotubes (SWCNTs) suitable for biological sensor and drug delivery applications. Their desirable optical properties such as indefinite photostability, high spectral diversity, and near-Infrared (nIR) fluorescence make them sensitive to their local electrostatic environment [3] and suitable for biomedical applications. Thus, many recent

in *in vitro* and *in vivo* sensing and imaging applications using SWCNTs are demonstrated [2,4–9].

In recent years *in vitro* nanoparticle testing under static cell culture conditions is increasingly compared to flow conditions under shear stress [10–13]. Shear stress is an important and ubiquitous biomechanical parameter concerning *in vivo* conditions. To mimic *in vivo* conditions, microfluidic flow chambers are used with the intention to apply defined physiological flow to the mammalian endothelia cell line A549. Cancer cells experience two main types of fluid shear stress [14]. On the one hand low shear stresses, generated by interstitial flow in their microenvironment, which are likely to occur between *in vivo* cancer cells [15]. On the other hand, higher shear stresses, which occur on endothelia cells in the venous vasculature system [16,17]. As a result of the common epithelial structure of A549 and endothelia cells in the inner layer of blood vessels, the experimental set up of this thesis can also be understood as an approximation of a blood vessel model. Therefore, the findings of this study can also relate to adsorption and desorption effects of SWCNTs in blood vessels. The novelty of this study lies in the method of using hyperspectral nIR imaging of SWCNTs under flow in a microfluidic chamber. The variation of mass flux in the chamber to investigate the influence of shear stress on the adsorption, desorption and uptake of SWCNTs of A549 cells are also not presented in the scientific literature. These aspects are valuable for the efficient use of SWCNTs for drug delivery and biosensing approaches.

CHAPTER 2:   BACKGROUND

This section contains background information in addition to the main elements of the conducted experiments in this thesis. It includes theoretical knowledge about the used nanoparticles, the cells, particles coronas, flow characteristics and associated dimensionless numbers.

2.1 Carbon Nanotubes (CNTs)

CNTs are cylindrical structures of sp^2-hybridized and covalent linked carbon atoms [18]. CNTs belong due to their structure of pentagonal and hexagonal rings, (see Figure 2.1) to the group of fullerenes. A various number of rolled graphene sheets represent the so called multi-walled carbon nanotubes. In the case of only one existing sheet the carbon nanotube is called single walled carbon nanotube (SWCNT).

2.1.1 Single Walled Carbon Nanotubes

The diameter of single walled carbon nanotubes (SWCNTs) can ranges from approximately 0.5 nm to 5 nm [19] and the lengths of the tubes can range from 10 nm to 10 μm. A representative SWCNT, which is similar to those used in this thesis project, is shown in Figure 2.1.
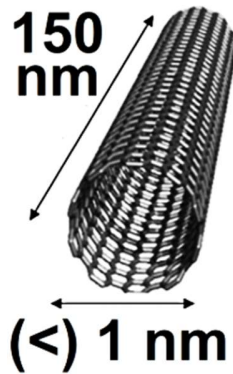
Figure 2.1: SWCNT with scale bars

Favorable SWCNT properties, including environmentally responsive electric, optical, and colloidal behavior, the ability to modify and functionalize their surface, make SWCNTs uniquely suited for biological sensing and drug delivery applications. SWCNT optical properties are particularly interesting and include indefinite photostability, high spectral diversity, and near-Infrared (NIR) fluorescence that make them suitable for *in vitro* and *in vivo* applications [2,4–9]. In this promising field of imaging and biosensing, there is room for improvement concerning limited dynamic range, response time, and signal photobleaching and quenching [20,21].

2.1.2   SWCNTs functionalized with single-stranded DNA

A basic requirement for using SWCNTs in aqueous solvents, is the improvement of the solubility of SWCNTs and of the biocompatible with body fluids, so they elicit few toxic side effects [22]. The used SWCNTs have an average length of 150 nm, diameter of < 1 nm, and are functionalized with single-stranded DNA (ssDNA).
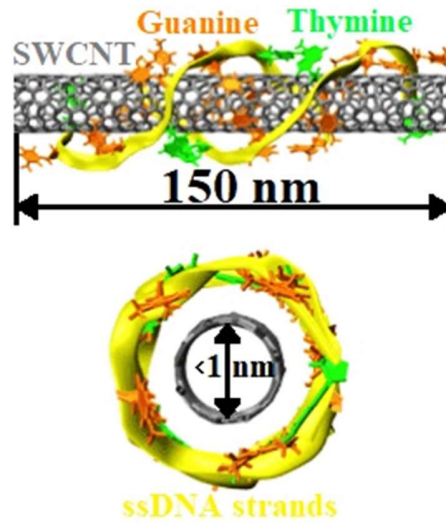
Figure 2.2: Site and front view of (GT)₁₅ SWCNT, wrapped with ssDNA *[23]*

These nanoparticles are processed SWCNTs, which are complexed with short DNA strands. As determined by the abbreviation $(GT)_{15}$, the DNA strand consists of 15 pairs of the nucleobases Guanine-Thymine. These attached ssDNA strands are each 30 bases long with the sequence of 5′-GTGTGTGTGTGTGTGTGTGTGTGTGTGTGT-3′ and lead to the most efficiently dispersed SWCNTs [24]. There are multiple ssDNA strands per CNT (>10 strands), and the DNA non-covalently adheres to the surface of the SWCNTs through van der Waals forces and overlapping pi orbitals. The DNA adheres with a force of 10 kT per base, so 300 kT for $(GT)_{15}$. Therefore, unless something is actively displacing the DNA from the SWCNTs, it is stable on the SWCNT. External measurements of Atomic Force Microscopy (AFM) regarding the size of these DNA strands showed, that they have an approximate height of 0.5 nm and length of 20 nm. This is important in the context of this thesis, because the interactions of SWCNTs with biological tissues are investigated, where the exact size and the surface properties have a great influence.

5

2.2 Human lung carcinoma cell line A549

Many SWCNT work in the nanomedical field has been focused on cancer treatment and their use as delivery vehicles. Cancer cell properties vary significantly between different diseases, and understanding these variations is important for designing specific SWCNTs for each cell line. There are existing many different types of cancer cells, originating from varying tissue with differing mutations. In this context the scope lies mainly in carcinoma cells [25].

The cultured human lung carcinoma cell line A549 (ATCC® CCL-185™) belongs to the group of alveolar epithelial cells. This cell line has been widely studied and represents a model cell line. With an estimated number of estimated 234,030 cases in the US (2018), lung cancer is the second most common cancer in both men and women and creates the need of a therapeutic approaches [26].

These A549 cells grow adherently as a monolayer *in vitro* as well [27]. This specific type of epithelia forms the wall of alveolar sacs in the lungs and lines also the inner surface of all blood vessels (endothelium) [28]. Previous investigations with confocal microscopy determined the size of A549 cells to be approximately 40μm x 20μm x 10μm [29].
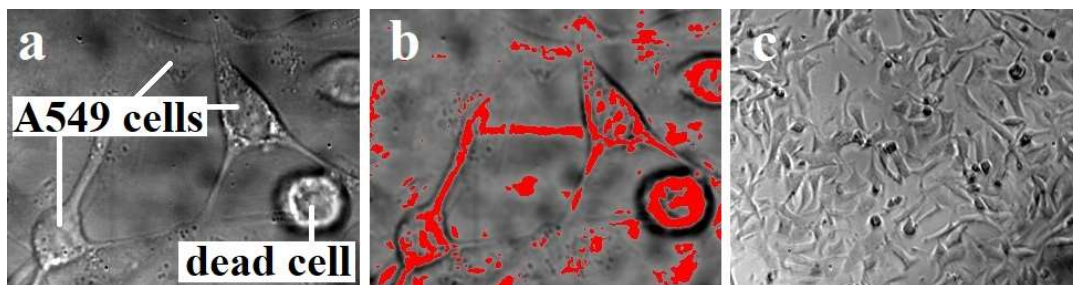
Figure 2.3: White light microscopic images of A549 cells. (a) 100x, exposure time 0.1s;(b) 100x, exposure time 0.1s with highlighted cells; (c) 20x, exposure time 0.02s

As shown in Figure 2.3, in a healthy state the cells form elongated shapes with stretching "arms". Whereas dead cells form round spheres and detach from the bottom of the flow chamber.

2.3 Cellular uptake of SWCNTs

Especially in terms of drug delivery and cancer-targeted nanoparticles vehicles, but also in biosensing purposes, a general understanding about their targeting and internalization mechanism into cells is crucial. There are different pathways of nanoparticle internalization, which can mainly be distinguished into active (energy dependent) and passive (energy independent) transport mechanisms. With and without ligand-mediated targeting, SWCNTs have been shown to display some of the highest tumor uptake values of all intravenously injected nanoparticles [30,31]. In the following two sections two general internalization pathways are introduced, based on the current status of scientific literature.

2.3.1 Endocytosis

Cellular uptake of nanoparticles is found to involve endocytosis for the majority of cases.[32–36]. Karimi et al. [18] described this discovery, which is more applicable in this context of using $(GT)_{15}$ SWCNTs. The cellular uptake of SWCNTs with DNA functionalized surfaces generally takes generally energy-dependent endocytosis pathways. Lee`s results also show that endocytosis is the main mechanism for ssDNA targeting into the nucleus of Hela cells using CNT delivery [37]. Particularly for DNA wrapped single-walled carbon nanotubes with lengths less than 1 μm, the internalization mechanism is confirmed to be receptor-mediated endocytosis (RME) [1,38,39].

Several factors and parameters are crucial for the uptake of SWCNTs, including the length of the nanotubes, surface coating by different functional groups, the properties

of particular cell types, the preparation method of the CNTs, and their degree of aggregation [1]

2.3.2 Nano-needling

Due to their nano-needle shape, SWCNTs are believed to cross the plasma membrane and enter directly into the cytoplasm likely upon an endocytosis-independent mechanism without inducing cell death [40]. The shape and morphology of SWCNTs is correlated to the length and diameter of the particles. Previous studies showed the CNTs with a hydrodynamic diameter larger than 400 nm underwent internalization through endocytosis, whereas smaller single SWCNTs or SWCNTs bundles were able to enter by penetrating the cellular membrane [37,41]

2.4 SWCNTs Diffusion

The diffusion of SWCNTs is an important aspect in of this thesis. Especially in terms of SWCNTs movement in the flow chamber and the influence of Brownian motion on them. To describe diffusion of particles in a liquid suspension with low Reynolds numbers (Re) the following Stokes-Einstein equation (2-1) is advantageous [42]. The characteristic length (d_{eff}) is in this case equivalent with the radius of a spherical particle.

$$D = \frac{k_b \cdot T}{6 \cdot \pi \cdot \eta \cdot d_{eff}} \qquad (2\text{-}1)$$

Table 2.1: Parameters used in the Stokes-Einstein equation

Constant	Unit
Boltzmann`s Const. (k_b)	[J/K]
Temperature (T)	[K]
Dynamic Viscosity (η)	[Pa·s]
Charactersitic Length (d_{eff})	[m]
Diffusion Constant (D)	[m²/s]

2.5 Protein corona

In biological fluids specific layer of proteins on nanoparticles highly affect the particle uptake by cells [43]. Therefore, the effect of proteins on the internalization of SWCNTs is further on focused.

2.5.1 Definition

The binding of proteins on nanoparticles (SWCNTs) leads to so-called protein coronas around particles. This modification of the surface and the morphology influences the physicochemical properties and the complex interactions of the nanoparticle with the cell membrane.

With the terms soft and hard corona, there generally two different types of protein coronas, which can be distinguished. Even though these terms and their role in the field bio-nano-interactions are still elusive [44]. The soft corona is loosely and reversibly adsorbed on the nanoparticles (see Figure 2.4). The nature of this outer protein layer is considered to be the single most important parameter in determining the nanoparticle-cell interaction (Jin, Heller, und Strano 2008). In comparison to the soft corona, the proteins, which are building a hard corona are strongly bound to the surface of the nanoparticle [45,46]. Interactions between protein and nanoparticles with a dissociation constant K_d larger than 10^{-4} M can be classified as weak interactions (soft coronas), where nanoparticles usually bind little protein nonspecifically *in vivo*. With a desorption constant K_d between 10^{-5} and 10^{-7} M, the interaction is moderate, while a K_d less than 10^{-7} M indicates a strong interaction as they occur in hard coronas [47]
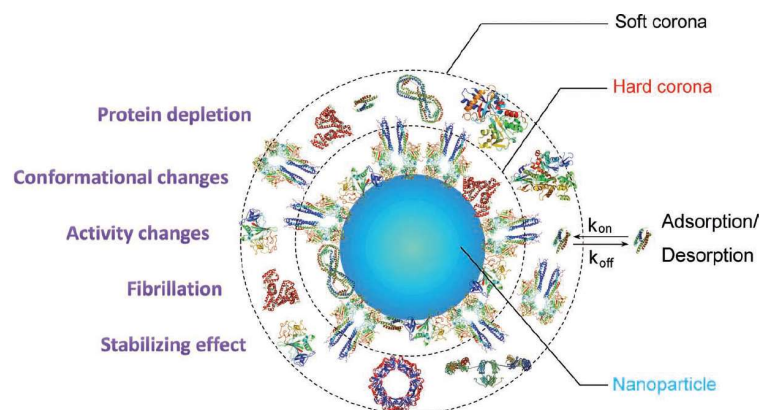
Figure 2.4: Protein corona on nanoparticles. Protein binding on the surface, causes series of consequences [47]

2.5.2 Fetal Bovine Serum and Bovine Serum Albumin

Fetal Bovine Serum (FBS) is the most universally applicable cell culture additive for the simulation of cellular proliferation and biological production [48]. FBS contains hormones, paracrine, endocrine and autocrine growth factors and rich variety of proteins which support cell growth [49].

The total concentration of proteins in FBS is 3.8 g/100 mL. With a proportion of 2.3 g/100 mL is Bovine Serum Albumin (BSA) the major protein of FBS and therewith one major compound. The glycine and isoleucine content of BSA are lower than in the average protein. Bovine serum albumin owing to high stability, availability in high purity form and excellent water solubility is suitable for attachment studies [50].

The protein Bovine serum albumin is very similar to the human serum albumin (SA). The only detailed compositional difference is that BSA has two tryptophan residues comparted to SA, which has only one [51]. BSA is known as the most abundant

protein in mammal blood. The binding tendency of serum albumin is in addition to the mentioned model of Yang Shen-Tao, with a concentration of around 10^{-4} M [47].

2.5.3   BSA binding on SWCNTs

In several studies unfunctionalized SWCNTs are found to bind BSA molecules. Ge et al. [52] describes a uniformly coverage, while a variety of other authors observed inhomogeneous distributions of BSA proteins on SWCNTs.

It is notable, that adsorption of BSA is greatly affected by the pH of the solution. As the isoelectric point (IEP) of BSA is at pH 4.5–5.0, the protein BSA is negatively charged at neutral pH, which is mainly present in cell media, and positively charged under acidic conditions. [52]. The surface of the $(GT)_{15}$ is because the attached ssDNA stands also overall negative charged. This primarily argues against high binding rates of BSA on the used $(GT)_{15}$ SWCNTs.

2.6 Flow characteristics

There are different flow characteristics, which are crucial to be investigated with the intention to evaluate the ad- and desorption of SWCNTs at the A549 cells. In the two following paragraphs the two main flow characteristics in the flow chamber are introduced-the shear stress and the velocity profile. The Figure 2.5 illustrates the size of the flow chamber and visualizes the shear stress and flow profiles.
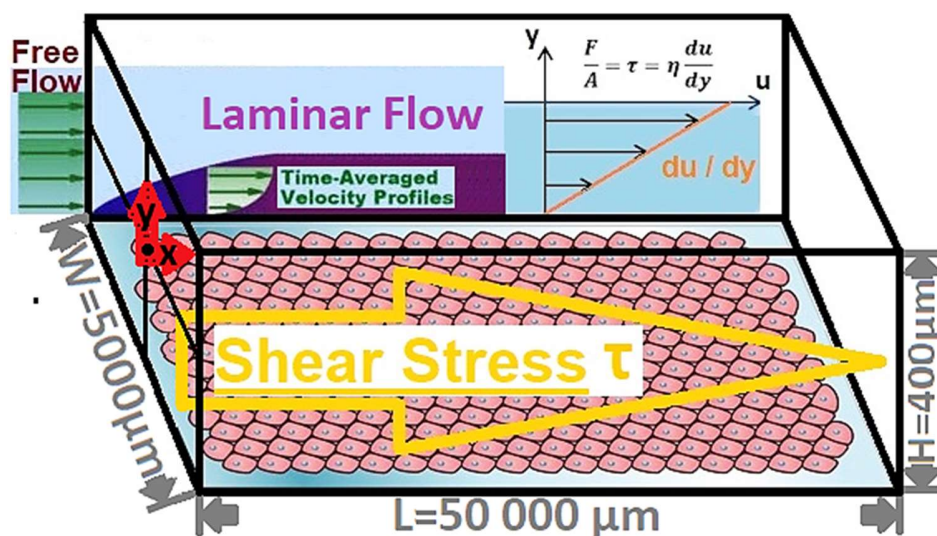
Figure 2.5: Illustration of characteristics of the fluid flow and of the flow chamber

2.6.1 Shear stress

Dependent on the morphology of the flow chamber and the flow rate, cells can experience different types of fluid flow. The shear stress τ plays a central role in the introduced system. Cell media is considered as a non-Newtonian fluid. Since the fluid flows over the cells with a specified velocity (v(x)), it forces the cells to deform in flow direction.

Shear stress in flow chambers are commonly measured in dyn/cm². One dyne is equal to 10 µN, 10^{-5} N. In terms of common epithelial structures between A549 cells

and the structural design of blood vessels, the goal is to set reasonably shear stress values in this study which mimic conditions in human blood flow and around tumor cells.

In addition to that, experimental measurements using different methods have shown that in humans the magnitude of shear stress ranges from 1 to 6 dyn/cm^2 in the venous system and from 10 to 70 dyn/cm2 in arteries [53]. Epithelia cells in small arteries and veins are exposed to constant laminar flow. Cancer cells are exposed to these range of hemodynamic shear forces in the venous bloodstream from 0.5 to 4.0 dyn/cm² [54]. Besides that, there is also interstitial flow on the cell surface, with shear stresses, which are believed to be in the order of 0.1dyn/cm² [14,55,56].

2.6.2 Calculation of shear stress and velocity profile

The actual local velocity v(x,y) in this rectangular flow chamber can be calculated with the following equation (2-2) [57]. Note, that compared to the coordinate system in Figure 2.5 the following equations show a z-coordinate, which is switched with the x-coordinate.

$$v(x,y) = -\frac{1}{\eta}\frac{dp}{dz}\left\{\frac{b^2}{2} - \frac{x^2}{2} - \sum_{n=0}^{\infty}\frac{(-1)^n(2b^2)}{(2n+1)^3}\left(\frac{2}{\pi}\right)^3\frac{\cosh\left[(2n+1)\left(\frac{\pi y}{2b}\right)\right]}{\cosh\left[(2n+1)\left(\frac{\pi h}{2b}\right)\right]}\cos\left[\frac{(2n+1)\pi x}{2b}\right]\right\} \tag{2-2}$$

Table 2.2: Parameters used in the equation (2-2) after Cornish

Constant	Unit
Hight (h)	[m]
Width (b)	[m]
Pressure loss (dp/dz)	[Pa/m]
Distance parallel to the axis (z)	[m]

Due to the fact, that A549 cells are attached to the bottom of the channel. The wall shear stress at the bottom of the channel (y=-h) and at the center of the channel (x=0) is calculatable with the following equation [58]:

$$\tau(x=0, y=-h) = \eta \frac{\Phi}{q} \left\{ \sum_{n=0}^{\infty} \frac{(-1)^n b\pi}{(2n+1)^2} \left(\frac{2}{\pi}\right)^3 \tanh\left[(2n+1)\frac{\pi h}{2b}\right] \right\} \tag{2-3}$$

After plugging in the dimensions of the used flow chamber (see. 3.3.1) the equation to calculate the shear stress at the bottom of the flow chamber can be simplified. This simplification with the factor 131.6 bases on the calculation with the showed units in equation (2-4). Therefore, the variables and can only be used in this shown units.

$$\tau = \eta \cdot 131.6 \cdot \Phi$$
$$\left[\frac{dyn}{cm^2}\right] = \left[\frac{dyn \cdot s}{cm^2}\right] \cdot \left[\frac{mL}{min}\right] \tag{2-4}$$

16

2.7 Dimensionless numbers

The flow of media can be described by using characteristic numbers. These numbers are used to characterize flow properties with the intention to compare flow conditions in between microfluidic channels. Especially the Reynolds-number (Re) is used to determine the fluid flow regime (laminar, transitional and turbulent) in the flow chamber. Reynolds-numbers close to zero (Re << 1) indicate strongly laminar flow. Turbulent flow can only occur at high Reynolds-numbers (Re > 10^3) [59].

The distinction between convection and diffusion mass transport of the SWCNTs in the flow chamber is a central point in this thesis. Therefore, the Peclet-number (Pe) is used. In most common microfluidic cases, convective transport is faster than diffusive transport (large Peclet number), even though the length scales of the flow chamber are small. The following range for Pe is applicable for flow chambers: $10 < Pe < 10^{-5}$ [60].

Another dimensionless number, which can be used to characterize flow conditions, is the Schmidt-number (Sc), which represents the ratio of viscous diffusion rate and the molecular (mass) diffusion rate. It physically relates to the relative thickness of the hydrodynamic layer above the cancer cells and mass-transfer boundary layer [61].

2.8 Hyperspectral imaging

Hyperspectral imaging deals with the electromagnetic light spectrum, even in the invisible spectrum for the human eye and in each single pixel of an image [62]. Hyperspectral imaging uses continuous and contiguous (wide field) ranges of wavelengths in the step size of 0.1 nm. In contrast to multispectral imaging with the step size of 20 nm [63].

2.8.1 NIR hyperspectral microscopy of SWCNTs

Single-Walled Carbon nanotubes (SWCNTs) offer with their introduced properties an intrinsic opportunity to analyze their interactions with biologic tissues. Regarding this, the emitted fluorescence of carbon nanotubes can be detected with near-infrared (nIR) detectors. InGaAs (indium gallium arsenide) detector, the change of the fluorescence intensity, wavelength or spectral bandwidth due to environmental influences can be detected and evaluated. These signal responses make it possible to use SWCNTs as optical sensors. In addition to binding processes of defined molecules these optical signals change specifically. In the recent years, several nanotube-based optical sensors were developed for detecting small molecules [21], neurotransmitters [64], oxidative radicals [65] and macromolecules [66].

In the context of this thesis, broadband nIR fluorescence images were acquired and analyzed, neglecting the need for hyperspectral imaging. A more detailed overview about this method is given by Roxbury et al. [67].

2.8.2 Alternatives to hyperspectral imaging under flow

The approach of investigating SWCNTs flow with an nIR fluorescence hyperspectral microscope is minimally represented in the scientific literature. Most sources with similar topics use confocal microscopy [13,68]. The hyperspectral flow cytometry also focuses mostly on fluorescence of the cells and is able to detect SWCNTs in flow conditions.

Literature, which followed similar goals and methods like Broda et al. mentions, that with an increasing shear rate and flow rate, the number of adsorbed particles is increasing [68]. Farokhzad et al. showed that particle size and the type of nanoparticle has a greater impact on the adsorption on cells, than shear stress of the fluid has [69].

CHAPTER 3:   MATERIALS AND METHODOLOGY

In the following section the development of the experimental set up and the implemented procedures are described. In the beginning, the processed SWCNTs are introduced as well as the applied cell culture techniques.

3.1 Single Walled Carbon Nanotubes: GT 15

The experimental investigations of this thesis are conducted with $(GT)_{15}$-SWCNTs based on TUBALL™ Raw-SWCNTs (OCSiAl, Luxembourg). Probe-tip sonication was used to enable the debundling of SWCNTs and non-covalent attachment of the DNA to the surface of the SWCNTs. The resultant dispersion was ultracentrifuged for 30 minutes at 250,000 xg, to remove undispersed SWCNTs and impurities, and the top ¾ of the supernatant was collected and used for the flow cell experiments. The resulting stock dispersion of $(GT)_{15}$-SWCNTs ($c_{(GT)15}$ = 204.5 mg/L) was determined to be at a concentration of 204.5 mg/L in terms of weight of SWCNTs [67] and was stored in the refrigerator during this time (2.5 months).

3.2 Cell culturing

In the following paragraphs, the applied three methods of cell culturing are described.

3.2.1 Cell splitting into flasks

The primary task during the cell culture phase is to keep the cells alive and healthy. In this manner cells were passaged every 2-3 days (see 6.6.1). To retain the genetic integrity of the cell line, the maximum number of passages for the A549 cells was limited to 30.

3.2.2 Inoculation of flow chambers

The inoculation of the flow chamber was conducted by taking the requirements of the manufacture specifications [70] into account. The most important details are the inoculation concentration of A549 cells, which was added into the flow chamber ($\sim2\cdot10^6$ cells/mL) and the period of time between inoculation and experiment (~48 h). The cell concentration was set by using the Cellometer Mini (Nexcelom Bioscience®, USA). The detailed procedure for the inoculation of the flow chamber is listed in section 6.6.

3.2.3 Cell Media and Serum Free Media

The composition of media plays an important role in the conducted investigations. There are two different types of media, which differ by the component Fetal Bovine Serum (FBS). The "complete media" (containing 10% FBS) was used for the cultivation and cell growth of the cancer cells and in the experiments. In comparison, "serum free media" (no FBS) was only used in experimental phases (see 3.4.3). The compositional difference is shown in Table 6.4.

3.3 Experimental set-up

To investigate the interactions between SWCNTs and A549 cells under flow and shear conditions, a flow chamber is used in the presented experimental set up (see Figure 3.1). This set up consists of 3 major components, which are introduced in the following paragraphs.
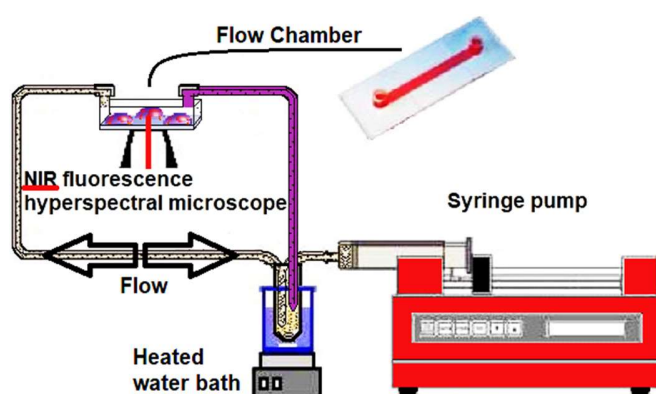
Figure 3.1: Experimental set-up of flow chamber investigations

3.3.1 Flow chamber

For experiments under flow conditions sterile ibiTreat µ-Slide l$^{0.4}$ Luer (ibidi GmbH, Germany) flow chamber was used. Compared to glass slides, which are mostly used for high resolution microscopy, this flow chamber is made of plastic (optical microscopy polymer). The variation of the refractive index ($n_{D, 589 nm}$ =1.52) with different wavelengths is represented by the Abbe number and is 56 for this optical polymer. Therefore, the flow chamber is well-suited for high resolution microscopy and shows similar signal-to-noise ratio as glass slides [70]. The geometric specifications of the flow chamber are listed in Table 3.1 and illustrated in Figure 2.5.

Table 3.1: Geometric specification of μ-Slide l$^{0.4}$ Luer Flow Chamber

	Dimensions	Unit
Length	50	mm
Width	5	mm
Hight	0.4	mm
Growth area	2.5	mm²
Channel volume	100	μL
Reservoir volume	60	μL

The bottom surface of the flow chamber is physically modified (Tissue culture treated surface-ibiTreat). This coating with biomolecules reduces the hydrophobicity of this surface and improves cell adhesion and growth.
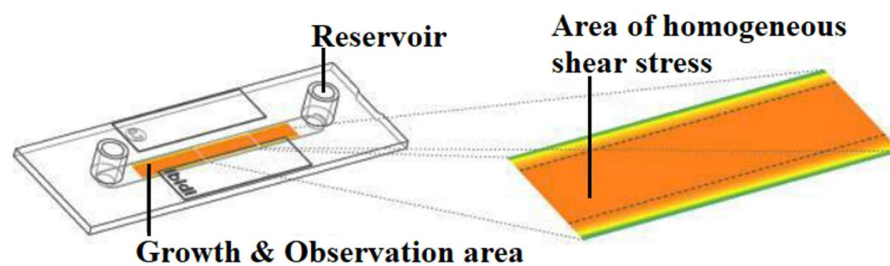
Figure 3.2: Shear stress conditions on the bottom surface of μ-Slide l$^{0.4}$ Luer flow chamber

3.3.2 Syringe pump and tubing

The flow of fluid is created by using the syringe pump NE-4000 (New Era Pump Systems, Inc, USA), which holds one 5 mL syringe. The plumbing consisted of the tubes with inner diameter of 1.6 mm and adapters for the connection between the ibidi μ–Slide (female luer) and the tubing of the pump. The corresponding tubes had a length of 90 cm in between pump and flow chamber and 60 cm in between the flow chamber and the media reservoir

In order to use cell media efficiently, the pump was programmed (see Table 6.2) to change pumping direction every minute, independent of the flow rate. The fluid is pumped with a constant flow rate to create the declared shear stresses (Table 3.2.)

Table 3.2: Main Shear stress and flow rates settings of experimental set-up

General flow settings	Shear stress τ [dyn/cm^2]	Flow rate Φ [µL/min]	Flow type [-]
Low	0.1	110	Interstitial
Medium	1	1060	Venous
High	2	2110	Venous

There are three general flow settings: low, medium and high. These shear stress values were chosen to mimic specific flow conditions in the human vascular system (compare 2.6.1). The intention behind the applied low shear stress is to simulate interstitial fluid flow around A549 cancer cells. Interstitial flow is the convective transport of fluid through tissue extracellular matrix [15]. It is believed that tumor cell surface shear stresses are on the order of 0.1 dyn/cm^2 [55,56]. The medium shear stress of 1 dyn/cm^2 and high shear stress of 2 dyn/cm^2 are typical conditions which can be found *in vivo* venous vascular systems [53,71–73].

3.3.3 NIR fluorescence hyperspectral microscope

In terms of imaging of SWCNTs and tissue cells the inverted near-infrared fluorescence hyperspectral microscope IX73 (Olympus, Japan) was used.
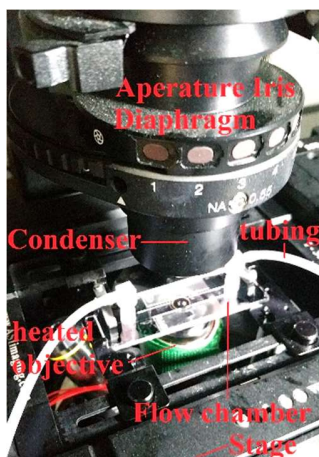
Figure 3.3: Flow chamber on the lens of the hyperspectral microscope

The flow chamber with its containing cells was centrally positioned on the lens of the NIR Hyperspectral Microscope (see Figure 3.3). Two light sources were applied in the experiments-halogen white light and a 1.5-Watt NIR laser, which emits monochromatic light at a wavelength of 730 nm. The objectives used had 20x and 100x magnification. The images of the NIR hyperspectral microscope were only quantified for fluorescence intensity of the SWCNTs. The operating temperature of the nIR camera (Xenics nv, Belgium) was -40 °C, which was ensured with gaseous nitrogen (N_2). Nitrogen was also used for the damped (High Performance Laminar Flow Isolator-I-2000 Series) optical floating table RS2000 (Newport, USA), which stabilized the table by absorbing vibration energies and thus supports consistent quality of microscopic images.

Dependent on the procedures (see section 3.4), different microscope settings were applied for imaging (see Table 3.3).

Table 3.3: Microscope settings of conducted procedures, using IMA™-IR (IR) & white light (WL)

Procedure	Magnif-ication	Light source	Exposure time	Details
	[-]		[s]	
Flow velocity profile analyses	100 x	IR	0.1	Motorized focus: Enabled, Filtering mode: Broadband Detector mode: High gain
Cell coverage	20 x	WL	0.02	
Cell intensity analyses **1st phase: Adsorption** **2nd phase: Desorption** **3rd phase: Uptake by cells**	100 x	IR	0.1	
Dispersion intensity analyses	20 x	IR	0.1	

3.3.4 Heating plate

To keep the temperature of the fluid in the flow chamber at 37 °C, the heating plate was set to 55 °C (131 °F). At this temperature, the stirred water bath (80 mL) transfers enough heat to the immersed tubing (20 cm). These settings resulted from preliminary studies under same conditions as the conducted experiments.

3.4 Experimental and evaluation procedures

In this section, the applied procedures are introduced. These are important due to potential errors and interpretations of the experimental data.

3.4.1 Flow velocity profile analyses

To characterize the velocity profile in the flow chamber, the fluid velocity is measured by detecting the nIR fluorescence of the SWCNTs and tracking them with variation of volumetric flow. The variation consists of 8 flow rates (2, 4, 6, 10, 20, 30 40 and 50 µL/min). For each flow rate, there were 15 videos of flowing SWCNTs recorded for 30 seconds. These 15 videos (cubes) differ in the z-position (height) inside

the flow chamber, starting from the surface of the slide and moving into the liquid. The step size in the z-direction was 1 μm. This experiment was conducted with the intention to analyze the velocity profiles by using a sterile flow chamber and without any attached cells.

The particle tracking was implemented by using the ImageJ plug-in TrackMate. In the evaluation process, it was ensured that in each image of the video 65-70 particles were detected at every time point. Therefore, the DOG detector mode was used with a blob diameter of 1 μm, a linking distance of 2 μm and a threshold of 9.5. In total ~2500 particles were tracked in each video. The tracked particles moved not only in the x-direction through the flow chamber, but also in y-direction. Therefore, SWCNTs were mostly detected while crossing the majority of picture section. To ensure a defined focus of the moving particles, the exposure time was optimized to 100 ms.

3.4.2 Cell coverage

As determined by the inoculated cell concentration and other culture conditions, the cell growth achieved a specific cell coverage on the bottom of the flow chamber. This analysis relies on 20x white light images with corresponding resolution (see section 3.5.1). The developed procedure (see Table 6.6) is visualized in the Figure 3.4.

In addition to subtracting the white light background with the intention of normalization purposes, the Fast Fourier Transform (FFT) is used. The need for this option is based on the inhomogeneous background (compare Figure 3.4. a). Spots with locally changing higher intensities (higher frequencies) are caused by reflections and refraction of the white light. The Fourier Transformation is used to filter out the initial

white light image in the frequency domain. As visualized in Figure 3.4. c, the transformation of these frequency domains to complex imaginary numbers is needed to detect and sort these frequency clusters.
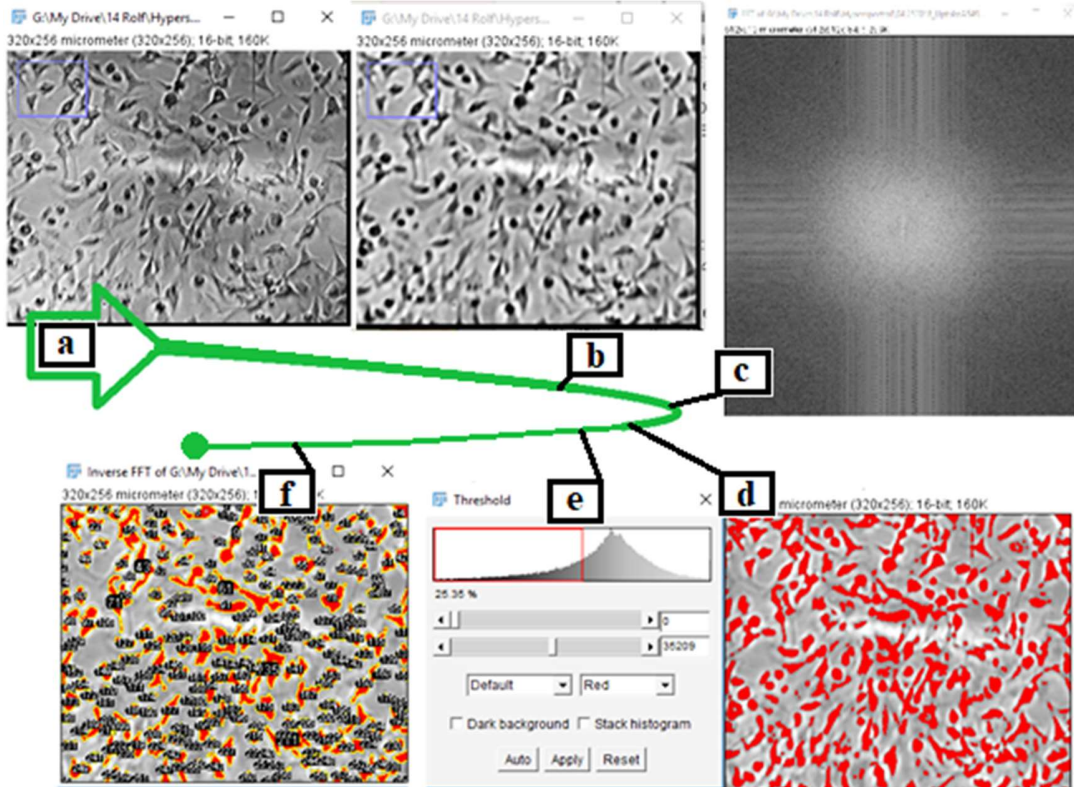
Figure 3.4: Illustration of evaluation steps in cell coverage analyzes. (a) initial white light image (20x); (b) Fast Fourier Transformation (FFT) applied; (c) Inverse FFT-Image; (d) Highlighted cells after using threshold; (e) Corresponding threshold controlling window; (f) Cell data map

The higher the frequency of the cluster is, the lager is their distance to the center of the Image [74]. With this principle, it is possible to cut out the higher intensity clusters from the background and evaluate the cells with lower intensities only. For each flow chamber, three images were evaluated.

28

3.4.3 Cell intensity analyses: Experimental phases

The fundamental objective to investigate the adsorption and desorption of SWCNTs on A549 cells, and also quantify the cellular uptake, leads to the development of three experimental phases. These respective phases are demonstrated in the Figure *3.5*, which shows with the phospholipid bilayer the cell-fluid interface. In relation to the following illustration, these phases are presented in the following paragraphs.
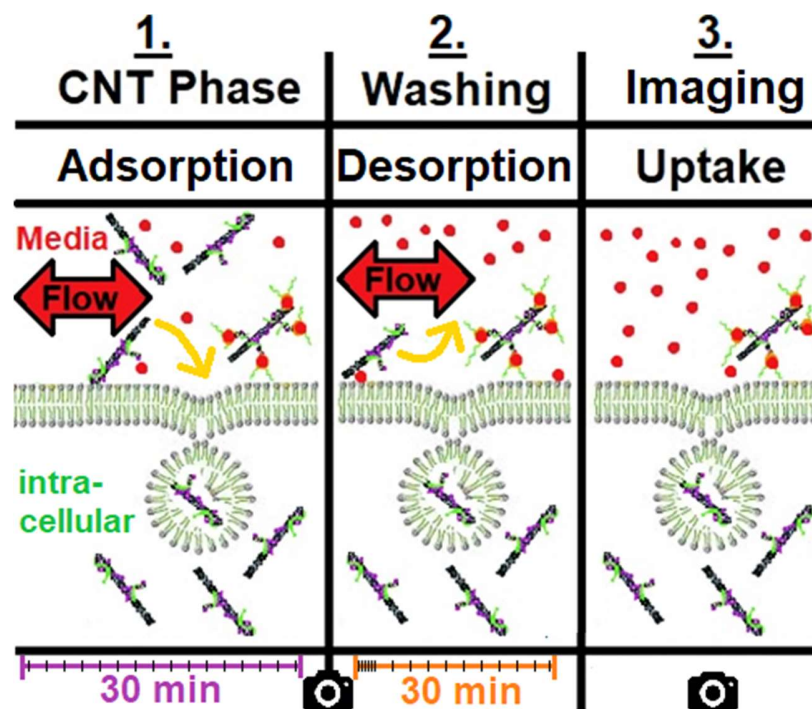
Figure 3.5: Illustration of the experimental phases on the celluar surface

CNT phase: Adsorption by cell intensities

In the first 30-minute phase, the dispersion of SWCNTs and media (with FBS ("M") or without FBS ("SF")) is flown through the flow chamber and over the cells. The SWCNTs are adsorbed to the cell. At this point, a distinction cannot be made between adsorption onto the surface and uptake (endocytosis) into the cells. The experiment started with turning on the syringe pump. After 30 seconds a homogenous velocity was assured, and the first NIR-image was recorded. In the second minute of the experiment no picture was recorded, because the direction of the flow changed and with it the position of the cells and the focus of the microscope. Every other ongoing minute (2:30, 4:30…) one image was recorded (15 images in total) at the same spot with the same cells (~5 cells). In this 30 minutes the focus on the carbon nanotubes in or on the cells was periodically checked and moved if necessary.

Washing phase: Desorption by cell intensities

The motivation behind the second phase is firstly to remove the suspended SWCNTs above the cell, and with it the fluorescence background. Secondly and more important in this washing phase is removing the SWCNTs that may be adhered but not internalized into the cells. In order to start the pump again for this second phase, some preparations had to be performed. The SWCNTs filled tubing were unplugged and replaced by tubing, filled with fresh media (dependent on the mode: M or SF). During this step, the flow chamber is moved marginally, so that the focus had to be moved again. Subsequently, the pump in this second phase was started again with the same flow rate as in the previous phase. Also, in this time-period of 30 minutes the focus on

the carbon nanotubes was periodically checked and if necessary refocused in z-direction. As indicated in the bottom of Figure 3.5, images were taken every 3 seconds in the first minute of this desorption phase. The reason for this is to observe the exact change in intensity when the SWCNTs are washed of the cell surface and out of the flow chamber. After 2 and a half minutes, images were recorded every other minute until 30 min elapsed, equivalent to the adsorption phase. The location of measurement was changed from phase adsorption to phase desorption, but within each phase the location was not changed.

Imaging Phase: Uptake by cell intensities

Finally, after washing the flow chamber with media (desorption phase), the stage was moved in x and y direction at constant z position to image more cells. About 10 different spots were recorded to get reliable intensity data, which should give certainty about the quantity of absorbed SWCNTs into the cells. Only 5 images, which showed an average intensity were selected, combined in a stack and evaluated.

Equivalent to this procedure there were also images taken after the adsorption phase and combined in a 5-images stack. In the end after all experiments were conducted, all stacks were combined in a "hyperstack" and evaluated. The reason behind this intricate and detailed method is that all these stacks must be applied by the same threshold (see 6.7.2) to achieve an accurate comparison of the intensity values.

3.4.4 Dispersion intensity analyses

Another applied method to quantify the amount of SWCNTs relies on the intensity difference of the SWCNTs dispersion before (initially) and after the adsorption or rather after desorption phase. It is important to distinguish this method from quantification of SWCNTs uptake by measuring the cell intensities (3rd phase: Imaging, Uptake phase). For this purpose, the following 4 samples of each experiment were measured 4 times.

- CNTs initial: Initial SWCNTs concentration
- CNTs after adsorption: SWCNTs concentration after adsorption phase
- Media initial: Media (M or SF) before without SWCNTs (Blank)
- Media after desorption: Concentration of detached SWCNTs in the media

Each sample was prepared by using a VORTEX mixer and pipetting a volume of 100 µL in a 96-well plate.

3.4.5 Variation of parameters

This thesis focuses on two central parts: (1) the influence of FBS and (2) the influence of shear stress on the adsorption, desorption and absorption of SWCNTs by A549 cells. The first part (FBS-focus) is accomplished by comparing the resulting data of complete and serum free media (see section 3.2.3). The influence of shear stress relates directly to the flow rate. Besides the shear stress, there are two other variable parameters-the media (M or SF) and the concentration of SWCNTs. The two modes of concentrations are hereafter called as the mode of concentration and the mode of constant mass flux. Table 3.4 illustrates these two modes. In the first mode, the constant mass flux represents the case that a constant mass of SWCNTs hits the cells, because

the mass flux is calculated to be constant with the value of $Q = 5 \cdot 10^{-5} \left[\frac{mg}{min \cdot mm^2}\right]$.

That means that the ratio between the bar charts of the concentration and the arrow of

flow rate is constant in Table 3.4. The exact concentrations $(c_1, c_{2,} c_3)$ are listed in the

sample preparation procedure in section 6.5. The second mode constant concentration

refers to the constant concentration of SWCNTs $c_1 = 0.91 \left[\frac{mg}{L}\right]$ in the dispersion. With

higher flow rates, the mass of SWCNTs hitting the cells increases with the shown factor

(light green colored).

Table 3.4: Overview of experimental design with two modes of SWCNTs concentrations c_1-c_3 with regard to the tree different flow rates f_1-f_3 resulting from the introduced shear stresses, considering two trials with media (M) and two with serum free media (SF) each.

There are six different charts in Table 3.4, but the first line for f_1=0.1 mL/min shows

the same setting. Hence, there is only one icon for M and SF. Consequently, there are

in total five different settings in the table. The experiments were conducted in replicate

to ensure the collected data with resulting conclusions. Therefore, every cell represents

four experiments, two for each type of media

3.5 Evaluation methods

All the experimental data in this thesis are extracted data from microscopic images. Thus, the evaluation methods are crucial to achieve meaningful and reliable data from the recorded images.

3.5.1 **Image J**

The image processing software used was ImageJ. The images were saved and processed in HDF5 format. With special attention to the velocity tracking, but also in general for judging the right length scale in all images, the resolutions of the two used magnifications (see Table 3.5) had to be inserted into ImageJ. Several plug-ins of ImageJ applied and described in the corresponding procedure sections.

Table 3.5: Resolution of hyperspectral microscope in dependence of magnification

Objective	Resolution	
	[µm/Pixel]	[Pixel/µm]
20x	0.301	3.32
100x	0.104	1.48

3.5.2 **Blanks**

To process the background-subtraction there is a need to record two images, which serve as a blank. For the first image the nIR laser was turned on and the sample (cells, media in petri dish or flow chamber) without any SWCNTs was imaged. The second image was taken of the same setting without nIR laser radiation (laser off). The nIR images are also called Broadband PL (BB)-Images.

3.5.3 **MATLAB**

Besides building stacks, also the background subtraction was performed by using MATLAB codes. The fundamental correction followed the procedure, presented in equation (3-1):

$$Background\ corrected: \frac{BB_{Raw} - BB_{off}}{BB_{on} - BB_{off}} \tag{3-1}$$

CHAPTER 4:   RESULTS

4.1 Flow characterization

4.1.1 **Simulated velocity**

The simulated velocities in the flow chamber include two ways of calculations. On the one hand the velocity calculation in a rectangular channel based on equation (2-2) after [57], and on the other hand the assumption of steady state plug flow in the chamber.

Velocity after Cornish

To calculate the local velocity v(x,y) in the flow chamber the dimensions of the chamber and the coordinates of the central location (compare Figure 3.3) in the flow chamber (x=L/2; y=0) were used. The calculation of the simulated data was conducted by using MATLAB. The calculated velocity profiles are similar to plug flow conditions. In terms of verifying the experimental data with this calculation, the approximate range of velocity matters.
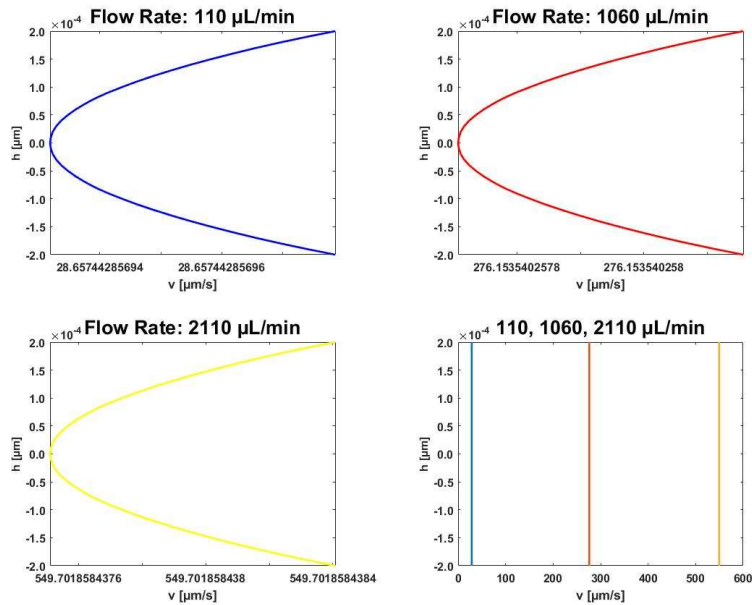
Figure 4.1: Simulated velocity profiles based on equation of [57] **in central point of the flow chamber independence of three flow rates, used in the cell intensity studies.**

Steady state plug flow

The continuity equation takes a steady state plug flow into account. This approach neglects the parabolic velocity profile with decreasing velocities near the surface of the flow chamber, due to friction. Higher flow rates effect the shrinking of boundary layers of the parabolic profile. The calculations of the plug flow velocities were performed by dividing the flow rate with the cross-sectional area of the flow chamber ($A = 2$ mm²). The resulting linear correlation is shown in Figure 4.3 and Figure 4.4.

4.1.2 Measured velocity

The velocities of the tracked particles at different flow rates are shown in Figure *4.2*. The highest flow rate 50 µL/min leads to the highest measured velocity of 25

µm/sec. Although the next smaller flow rate of 40 µL/min has only a difference of 10 µL/min less, the velocity data turned out to be similar to the corresponding of 50 µL/min. For the flow rates 30-50 µL/min, the scope of the graphs is generally decreasing with growing distance from the bottom so that a relatively constant and similar velocity values are presented at distances of ≥10 µm from the bottom. Even though that the flow rate is enhanced with the step size of 10 µL/min.

An increasing flow rate should physically lead to homogenous increasing velocities. That is the case for all investigated flow rates (2-30 µL/min). Therefore, the velocity differences are smaller with smaller step size in flow rates. It is notable, that at the bottom interface (distance = 0 µm) all curves show velocities around 15-17µm/sec. Even the very low flow rates of 2 µL/min and 4 µL/min show constant velocities around 17 µm/sec, independent on the distance from the bottom. These observations are results of the Brownian motion. The tracking of the small SWCNTs particles also detected the undirected movement of the SWCNTs. With this finding, it is to summarize that at low flow rates the Brownian motion has a notable and bigger impact on the motion of the small SWCNTs, compared to the movements initiated by the set small forces trough low flow rates in the chamber.
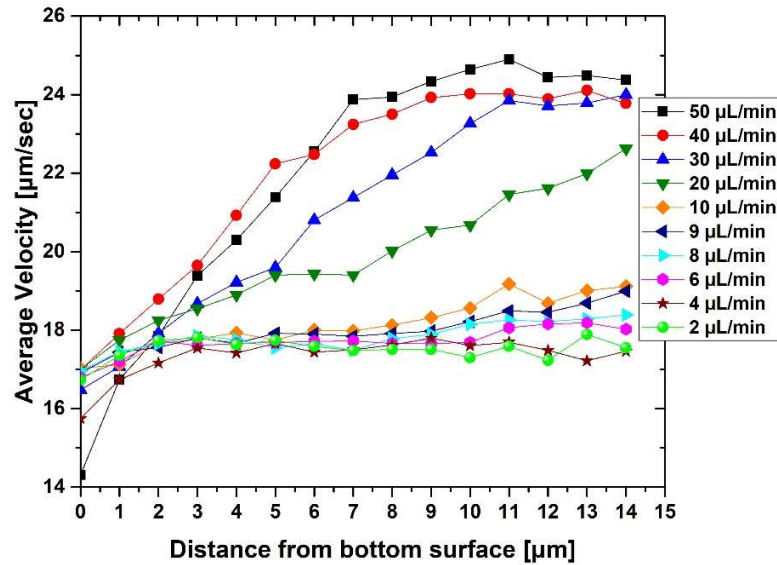
Figure 4.2: Measured velocities of SWCNTs in the flow chamber dependent on flow rates between 2 μL/min and 50 μL/min

Based on Figure 4.2 the Brownian motion can be quantified with an average two-dimensional projected velocity of approximately 17 μm/sec. The highest shown flow rate of 50 µL/min induces a shear rate of 7 s^{-1} for low flow rates and corresponding shear rates. Similar investigations of blood platelets with a diameter of 2 μm showed that for shear rates > 100 s^{-1} the Brownian motion is negligible for flow near a planar wall [75]. In comparison, the smallest applied flow rate in the conducted cell experiments was 110 µL/min (14 s^{-1}). In addition to the corresponding shear rate (14 s^{-1}<100 s^{-1}) the particles were also expected to show influences of Brownian motion (14 s^{-1}). The medium experimental flow rate (1060 µL/min; 139 s^{-1}) and high experimental flow rate (2110 µL/min; 278 s^{-1}) are believed to be independent of Brownian motion.

Reliable data without significantly influenced errors are found in between low flow rates (Brownian motion) and high flow rates (detecting limits). To extrapolate these

reliable flow rate data in the range of 10, 20 and 30 µL/min, the corresponding average velocities with the distances of 10 µm and higher from the bottom surface are used. The reason lies in the height of the A549 cells (approx. 10 µm) and the mostly constant velocities for the investigated larger distances. The extrapolated velocities are shown in the following section.

4.1.3 Comparison of simulated and measured velocity

It is important to compare the measured velocity data and the resulting extrapolated curve with the simulated data. Both, measured and simulated data lead to velocities without taking attached A549 cells into account. In addition to the experiments with A549 cells, attention should be paid to different surface roughness and consequential changes in the velocity profile.

In the following Figure 4.3, it is shown that the simulated data originating from continuity equation turn out with significantly higher values than the simulated data following Cornish and the measured data. The reason can be found in the fact that the continuity equation, considers plug flow and assumes a constant velocity profile. With this plot the significant difference of velocities from ideal continuity plug flow and flow near the planar bottom surface is established. Therefore, the conclusion supports the use

of the equation after Cornish, which considers the real conditions of lower velocities near the bottom surface.
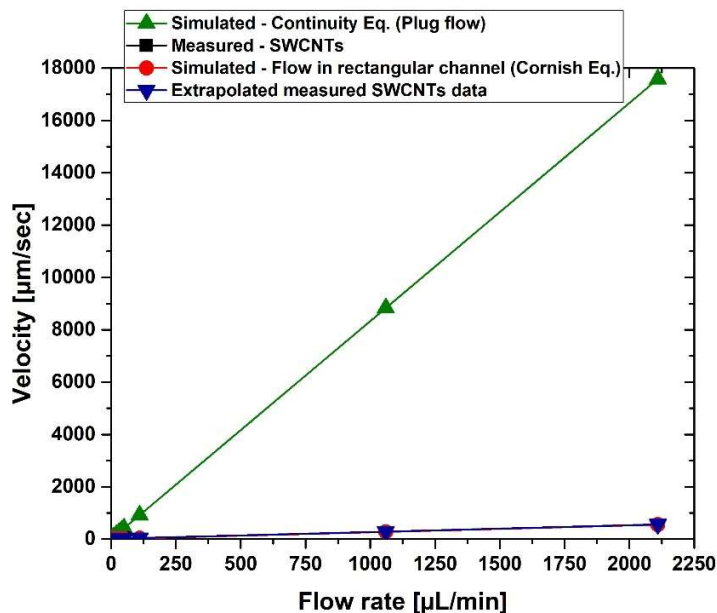
Figure 4.3: Comparison of all simulated, measured and linear extrapolated velocities

Both simulative approaches have in common that they are not considering the Brownian motion of SWCNTs, which was measured. As a result, the corresponding graphs of the simulated data start in the origin of the coordinate system. In Figure 4.4, the measured SWCNTs velocities and the extrapolated data are shown, which originate from the reliable measured data (see 4.1.2). Taking this for granted, the data of the flowrates 40 and 50 µL/min are lower than the extrapolated data in the positive x-axis direction, caused by the detection limitations of the SWCNTs. The measured data of lower flow rates < 10 µL/min agree relatively exact to the extrapolated data in direction of small flow rates.

41
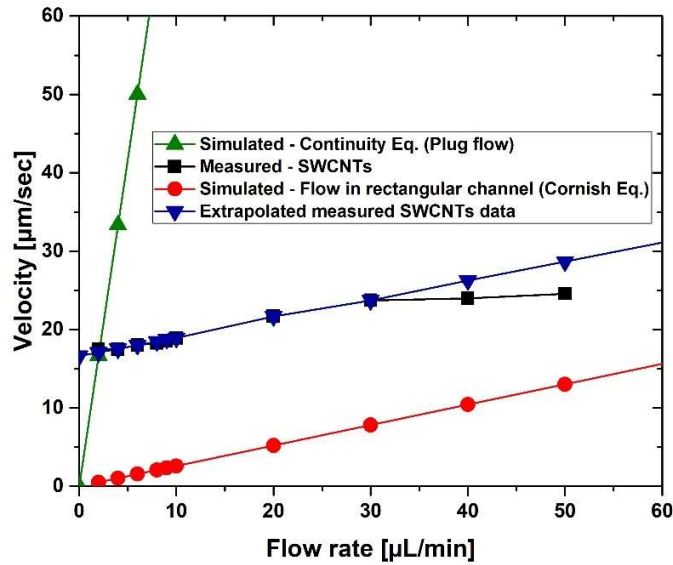
Figure 4.4: Comparison of simulated, measured and linear extrapolated velocities (< 60 µL/min)

The linear fit of the extrapolated measured data gives the linear equation of the velocities at the surface of the A549 cells (10 µm height) in the flow chamber.

$$v_{Extrapolated\_SWCNTs}(\Phi) = 0.2593 \cdot \Phi + 16.1777 \ [\text{µm/sec}]; R^2 = 0.99999 \qquad (4\text{-}1)$$

$$v_{Simulated\_Cornish}(\Phi) = 0.2605 \cdot \Phi + 0.00149 \ [\text{µm/sec}]; R^2 = 1 \qquad (4\text{-}2)$$

The slope of this linear equation for extrapolated velocities is similar to the slope of the simulated velocities after Cornish (compare Figure 6.10). In the double logarithmic plot, it becomes apparent that the extrapolation of measured data corresponds to the measured data at high flow rates and approaches asymptotically to the simulated data. These high applied flow rates and resulting velocities were not measurable by experiments.
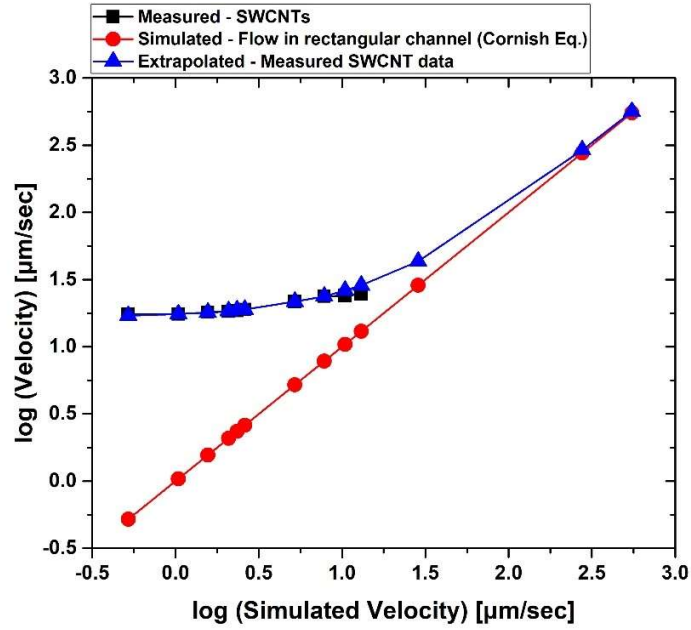
Figure 4.5: Double logarithmic plot of velocities over simulated velocities

The extrapolated fit in this plot of measured reliable data can be expressed with the following polymerically equation. Caused by the definition of the logarithm, the extrapolated and the simulated curve approaching to each other.

$$log(v_{Extrapolated}) = 4.07877 \cdot 10^{-5} \cdot log(v_{Simulated})^2 + 0.204787 \cdot log(v_{Simulated}) \, ; \\ log([\mu m/sec]); R^2 = 0.998 \tag{4-3}$$

On the bottom line, this double logarithmic plot demonstrated that the linear equation (4-1) combines the theoretical and experimental data. Consequently, these extrapolated data can be used to model the velocity of SWCNTs over the surface of A549 cells (distance from the bottom:10-15 µm) in the flow chamber, dependent on the flow rate of media at 37 °C in the introduced ranges. In other words, this specific analysis quantifies the influence of the Brownian motion at low flow rates and gives predictions for higher flow rates.

4.1.4 Diffusion coefficient

The diffusion coefficient plays a central role in the movement of the nanotubes. It is crucial to calculate the Peclet number to distinguish between advective or diffusive transport. In this context is becomes important in terms of SWCNTs adsorption and uptake. With the aid of equation (2-2) and the parameters shown in Table 4.1, the diffusion coefficient D is calculated. It is notable, that the characteristic length (d_{eff}) is calculated considering the size and the volume of one single $(GT)_{15}$-SWCNT.

Table 4.1: Parameters used in the Stokes-Einstein equation

Constant	Value	Unit
Boltzmann Const. (k_b)	$1.38 \cdot 10^{-23}$	[J/K]
Temperature T	310.15	[K]
Dynamic Viscosity (η)	0.0072	[Pa·s]
Characteristic Length (d_{eff})	0.000000002071	[m]
Diffusion Coeff. (D)	**$1.52 \cdot 10^{-11}$**	**[m²/s]**

4.1.5 Peclet-number (Pe)

The calculated Peclet-numbers indicate a clear result. Since all calculated Peclet-numbers are higher than 1, the convection in the flow direction is more dominant than transversal diffusion. The following bar charts provide the maximum and minimum values of all calculated Peclet-numbers considering the calculational method. The intermediate Pe-values are following the curve progression in Figure 4.3 and Figure 4.4, caused by the direct influence of the flow rate. The lowest measurement was taken at conditions with Pe in the order of 10^3. In comparison the Pe-values for the highest flow rates and shear stress were calculated in the range of 10^5 for experimental to 10^6 for

simulated data. Thus, the Peclet-number is about three orders higher than the corresponding Reynolds-number, which agrees to similar investigations by Guermonprez, Michelin, and Baroud [76].

4.1.6 Reynolds-number (Re)

The resulting Reynolds-numbers indicate a laminar flow, because all Re-values are in the range of 101 (see Figure 4.6, Figure 4.7). Especially on the surface of the cells, Re-values are close to 0. This is caused by smaller velocities near to the wall. In combination with the trackable SWCNTs in the flow chamber, this low Re-numbers lead to the result of homogenous flow conditions. In addition to literature in this field [77], this steady flow conditions are necessary to ensure quantifiable fluid shear stresses in the chamber and on the cells. These flow conditions enable the evaluation of SWCNTs interactions. Besides that, laminar flow mimics the natural surroundings of the cells, since the human blood flow is generally laminar [78,79].
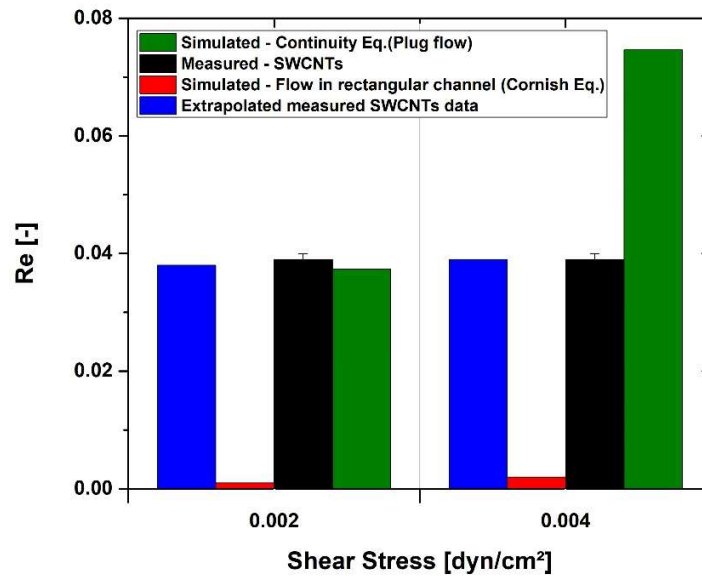
Figure 4.6: Re-values over shear stress resulting from the lowest flow rates 2 and 4 µL/min
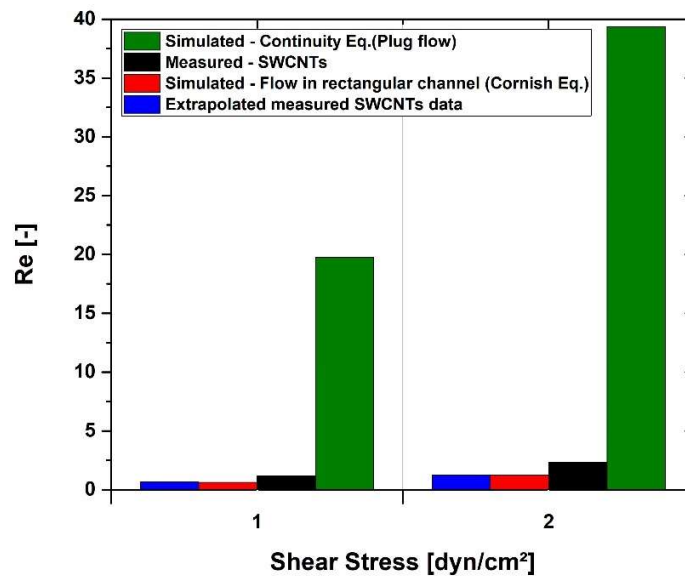
Figure 4.7: Re over shear stress resulting from the highest flow rates 1060 and 2110 µL/min

4.1.7 Schmidt-number (Sc)

After rearranging the equation (4-4) to Sc= Pe/Re, it becomes clear that Sc is a constant correlation factor which is applicable for all calculations. The ratio of Peclet- and Reynolds-number is determined to Sc = $4.73 \cdot 10^4$. This relatively high Schmidt-number indicates a thick hydrodynamic layer compared to the mass-transfer boundary layer. This points out that the fluid hydrodynamic movements of the fluid and the SWCNTs are dominant compared to their diffusive transport.

$$Peclet\ No.(Pe) = Schmidt\ No.(Sc) \cdot Reynolds\ No.(Re) \qquad (4\text{-}4)$$

4.2 Flow chamber characterization

The characterization of the flow chamber consists of the coverage with cells. This evaluation is important to ensure that the cells grow similar before the experiments were conducted. A difference of the number of cells influences directly the number of SWCNTs interacting with the A549-cells.

The following Figure 4.8 shows at the time of experiments, there were in average $1.2 \cdot 10^7$ ($\pm 0.25 \cdot 10^7$) A549-cells in the flow chamber. The standard deviation varies with the quality of the pictures. Overall it is notable, that the number of cells was in the order of 10^7 cells.
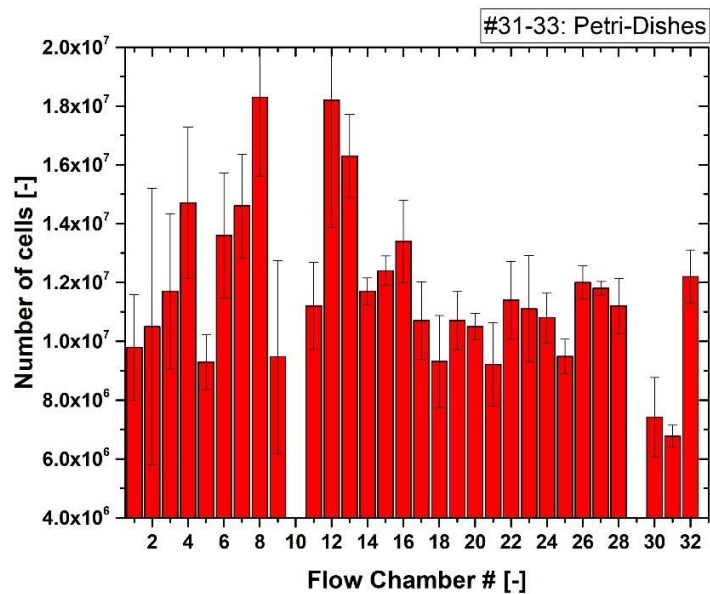
Figure 4.8: Number of A549 cells depending on the number of investigated flow chambers

Considering the total area of the chamber's bottom-surface (100 mm²), the relative chamber coverage with cells becomes ascertainable (see Figure 4.9). The average number of cells is therefore directly related to the average relative coverage of 37.3 % (± 9.1 %).
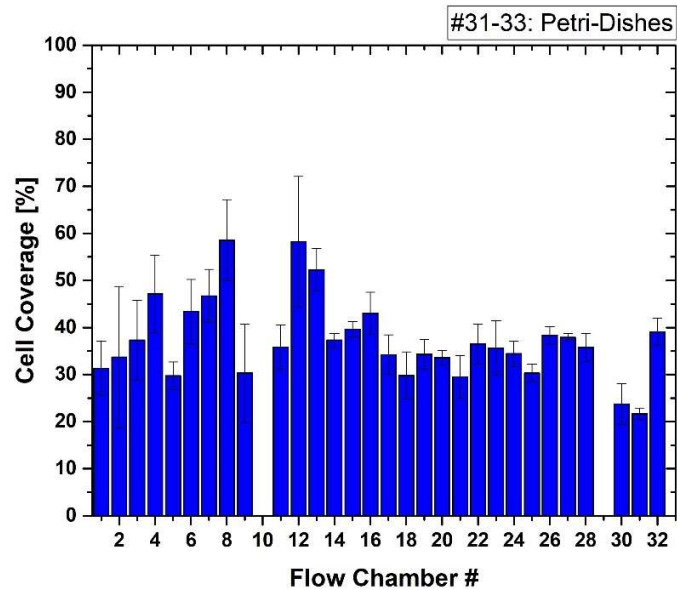
Figure 4.9: Number of A549 cells depending on the number of investigated flow chambers

To quantify the growth of A549 cells in the flow chamber, the ratio of the concentration, which was used at the inoculation, and the number of cells after 48 h of incubation was calculated (Figure 4.10). The hypothesis is that for the case of an inoculation with a high number of cells and a constant growth rate, there should be a higher number of cells after incubation.

The average ratio is 0.19 mL^{-1} ($\pm$ 0.05 mL^{-1}). The presented standard deviations of the average values to the value itself are similar in this section. The hypothesis of higher cell numbers after higher inoculation concentrations is refuted. That indicates, that the growth of the A549-cells is not only dependent on the number of cells (before and after incubation). That means in fact, that the growth relies on additional parameters like age of the cell culture, incubation parameters or limitations of growth factors in the media.

49
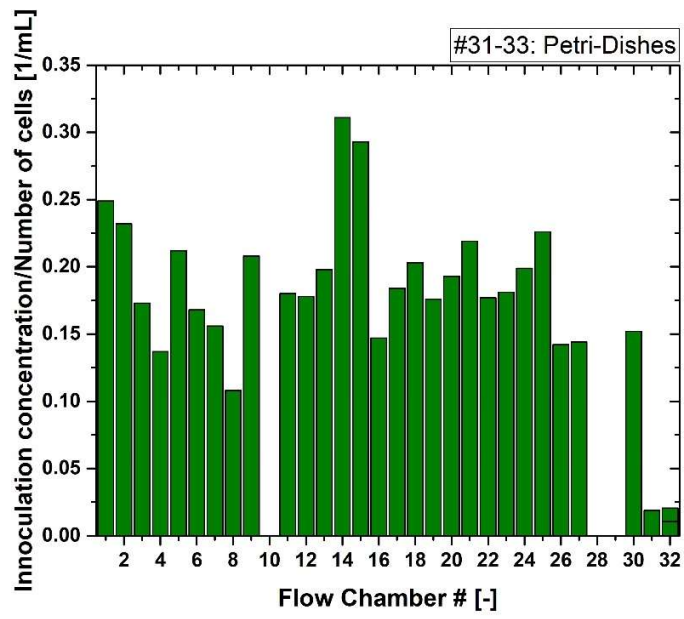
Figure 4.10: Number of A549 cells depending on the number of investigated flow chambers

4.3 Flow analysis: Constant mass flux of SWCNTs

The nanoparticle binding and uptake as a function of time is investigated by exposing A549 cells to constant mass flux of SWCNTs. The adsorption and desorption results are averaged data from duplicated experiments. The data were processed by using a sliding average of 3 values. In addition to this, the raw data are demonstrated in section 6.10.

4.3.1 Adsorption and Desorption phases

The overview of the results of the adsorption (0-30 min) and desorption (30-60 min) phase is given in Figure 4.11 The graphs show an overall a relatively small increase of SWCNTs intensity for the mode of constant mass flux.
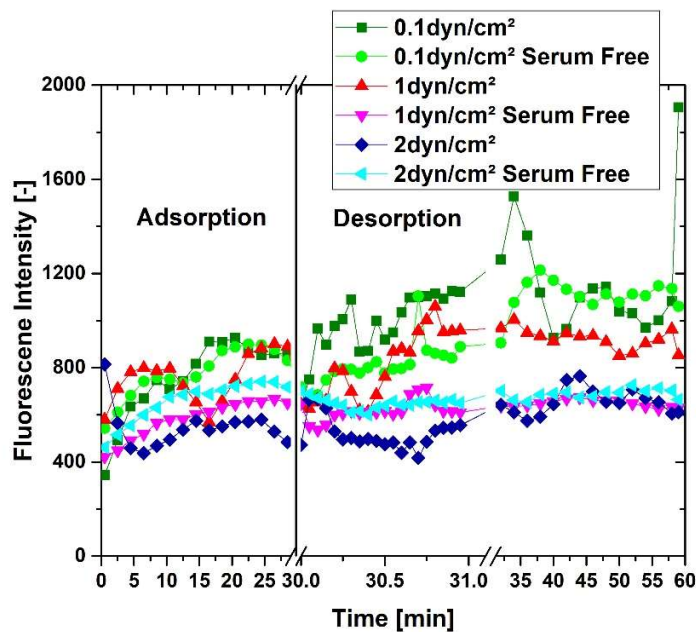
Figure 4.11: Intensity over time trough 3 experimental phases with constant SWCNT mass flux

This small increase is due to adsorption of SWCNTs on or into the cells. It is noticeable, that higher shear stresses show a smoother and more constant curve

progression. This effect can be explained by a much homogenously mixed dispersion of SWCNTs in media. At lower shear stresses in the chamber, aggregates can be formed more likely. These agglomerates can cross the picture section. This leads to outliers like after 35 min at shear stress of 0.1 dyn/cm².

4.3.2 **Adsorption phase**

An enlarged illustration of the results of the adsorption phase is given with the following Figure 4.12. While focusing the same spot of A549 cells, the fluorescence intensity of the adsorbing SWCNTs increases with time. The overall intensity is increased by ~150 relative units, independent on the shear stress. Taking the shear stress into account, the small shear stress of 0.1 dyn/cm² shows the highest increase of ~480 intensity units, which implied a doubling after 15 minutes of adsorbing SWCNTs. Focusing the average intensity of curves of each shear stress, the following vague tendency is observed. With higher shear stresses in the flow chamber, less SWCNTs seemed to get adsorbed on or internalized into the cells. This conclusion is supported by lower average intensity values at 1 dyn/cm² and at 2 dyn/cm². In comparison of the media and serum free media in terms of SWCNTs adsorption, there is no clear trend recognizable.
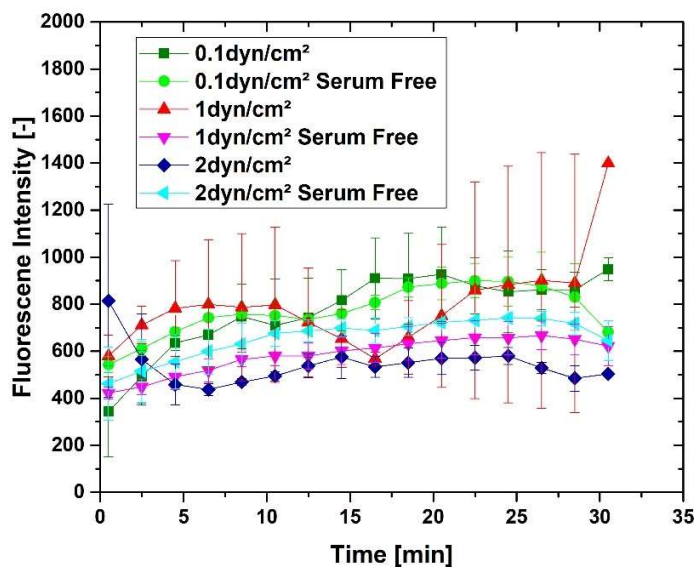
Figure 4.12: Intensity over time in the adsorption phase with constant SWCNTs mass flux

4.3.3 Desorption phase

The intensity values in the desorption phase are relatively constant over time. Despite the washing with pure media, there is no significant intensity decrease observed. This indicates that a neglectable amount of SWCNTs was desorbed of the cells. To conclude, the majority of SWCNTs have been internalized into cells or have not been removed from the membrane by the corresponding shear stress.

In general, the desorption phase in the mode of constant mass flux agrees with the mentioned analyses in the previous adsorption phase. Especially the fluctuations of intensity values in the conditions of low shear rates compared to high shear rates are also observed. Just like the smoother graphs for serum free data. The presence of FBS in the media could play a role in addition to the agglomeration of SWCNTs. This presumption becomes apparent regarding the data with FBS, which show higher

fluctuations than the data without FBS under the same shear stress. The trend from the adsorption phase is confirmed by the data in the desorption phase. At low shear rates the SWCNTs were internalized more likely than under higher shear rates. This effect is influenced by the binding energy of the SWCNTs on the negatively charged cell membrane. At high shear rates the forces applied by the flowing fluid must be larger than the binding forces, which prevents binding and detaches bounded SWCNTs from the membrane.
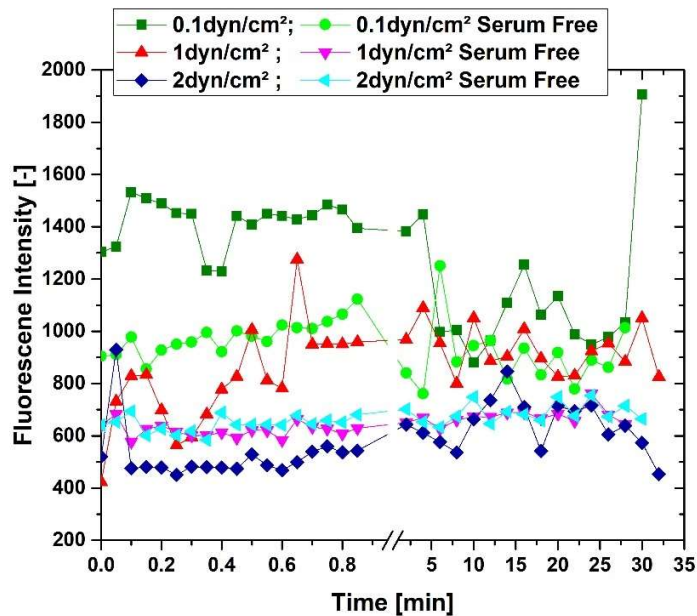
Figure 4.13: Intensity over time in the desorption phase with constant SWCNTs mass flux

4.4 Flow analysis: Constant concentration of SWCNTs

The nanoparticle binding and uptake as a function of time with respect to a constant SWCNT concentration in the dispersion leads to following results. Equivalent to the previously discussed mode "constant mass flux", the adsorption and desorption results of this mode "constant concentration" were also processed by using a sliding average of 3 values. The raw data are demonstrated in section 6.10.

4.4.1 Adsorption and Desorption phases

The adsorption and desorption results of experiments in this mode show significant differences compared to the previous introduced results in section Figure 4.3.
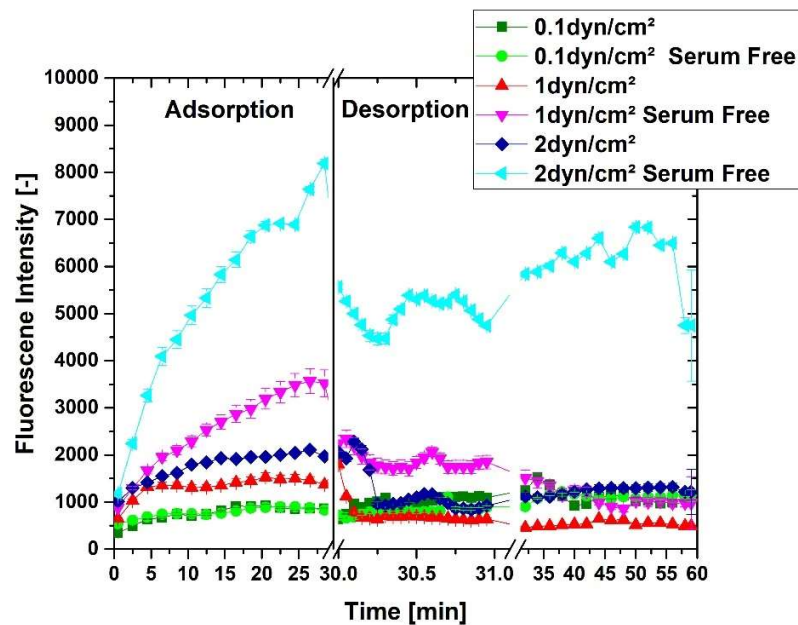
Figure 4.14: Intensity over time trough 3 phases with constant SWCNT concentration

The difference in orders of intensity values can be seen by comparing the results of medium shear stress (1 dyn/cm²) and high shear stress (2 dyn/cm²) in relativity to the

55

values of low shear stress (0.1 dyn/cm²). This is possible because the values of 0.1 dyn/cm² are the same as the corresponding in the mode of constant mass flux (Figure 4.11). It is notable that in this experimental mode, the collected data of higher shear rates show significant higher intensity signals (Figure 4.14). The graphs look smoother, which is also due to the larger scale on the y-axis.

Compared to this results in the mode constant concentration, the intensity values in the mode constant mass flux show no SWCNT-adsorption or-desorption depend on shear stress.

4.4.2 Adsorption phase

The detailed results of the adsorption phase (0-30 min) in this mode are shown in Figure 4.15. At this point it is notable, that the last data point (> 30 min) in the figure represents intensities of refocused images. The ideal focus for collecting the nIR signal of the SWCNTs differs between under flow and under static conditions. The data after 30 min experimental time show that the intensity decreases with adjusting the focus under static conditions.
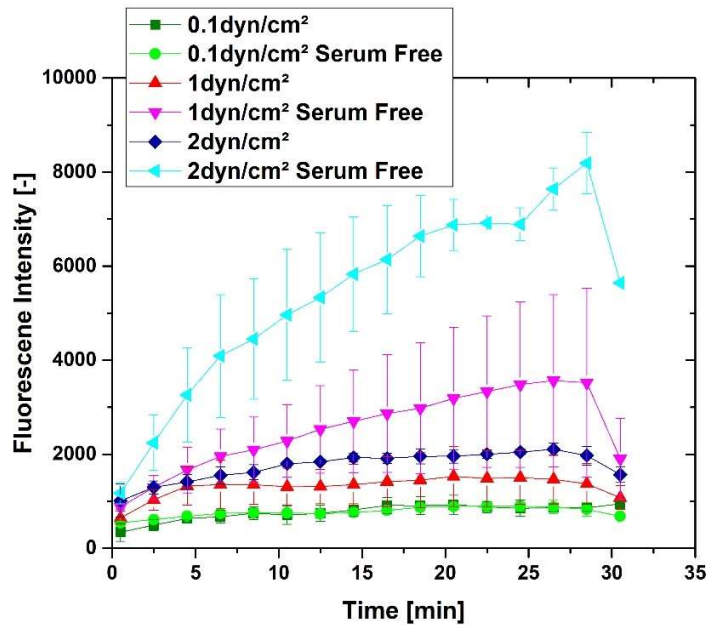
Figure 4.15: Intensity over time in the adsorption phase with constant SWCNT concentration

The constant concentration of SWCNTs in the media leads to higher intensities of the cells. With higher shear rates and flow rates is also the mass flux of SWCNTs in the chamber equally increased. In Table 4.2, the exact increasing factors of the mass flux are compared to the factors of averaged measured intensities.

Table 4.2: Ratios [-] of averaged adsorption intensities with regard to values of 0.1 dyn/cm²

Shear stress ratio	$\dfrac{1 \text{ dyn/cm}^2}{0.1 \text{ dyn/cm}^2}$	$\dfrac{2 \text{ dyn/cm}^2}{0.1 \text{ dyn/cm}^2}$
Factor of increased mass flux	**10**	**20**
M-Media (with FBS)	1.7	2.3
SF-Serum free media (no FBS)	3.3	7.0
SF / M	1.9	3.1

The averaged intensity increasing factors show that SWCNTs in media are adsorbed differently dependent on the presence of FBS. The experimental set up with an increase of 10 and 20 times higher mass flux suggests the duplication of SWCNT

adsorption. However, the averaged results show that at the highest shear stress (2 dyn/cm²), instead of 200 % only 135 % more SWCNTs were adsorbed in media dispersion than at the medium shear stress (1 dyn/cm²). This overall result agrees with observations in the literature [68]. Quite contrary to the adsorption of SWCNTs in the absence of FBS and its main protein BSA. The averaged serum free adsorption data show an increase of intensities of 214 % and agrees and even exceeds the expectations. This evaluation leads to the conclusion that FBS has an impact of the adsorption of SWCNTs under shear conditions. Lesniak et. al. confirms that a lower cellular nanoparticle (silica particles d = 50 nm) uptake of A549 lung cancer cells correlates with more proteins in the hard corona [43]. This leads to the conclusion that proteins, most likely BSA as the main compound in FBS, probably bind to the SWCNTs. As a result, a protein corona is most likely built, which increases the steric stabilization of the nanoparticle dispersion. Furthermore, the hydrodynamic diameter of the SWCNTs is increased, which is crucial for the cellular particle uptake. The presented results support this hypothesis by showing smaller internalizing rates of larger protein loaded SWCNTs than SWCNTs without attached proteins.
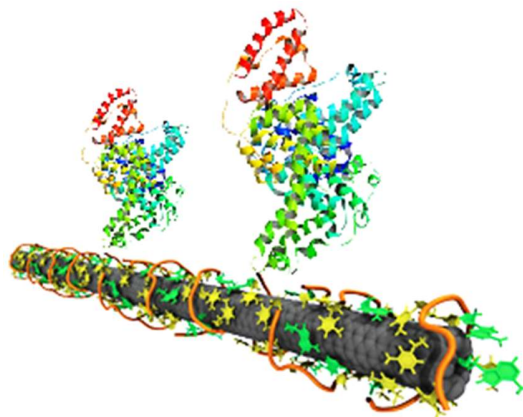
Figure 4.16: DNA-wrapped SWCNT with bound BSA proteins [80])

Data modeling:

The adsorption graphs can be modeled with the following exponential equation (4-5). The included constants are I_0, as the initial intensity, A as a proportion factor and R_0 as the adsorption coefficient.

$$I = I_0 - A \cdot e^{-R_0 \cdot t}$$

(4-5)

Table 4.3: Constant of fitted graphs distinguishing between media (M) and serum free media (SF)

	R_0		A		I_0	
	M	SF	M	SF	M	SF
0.1 dyn/cm²	0.15	0.09	586	370	897	909
1 dyn/cm²	0.37	0.05	935	3569	1426	4421
2 dyn/cm²	0.37	0.06	1123	7869	2082	8985
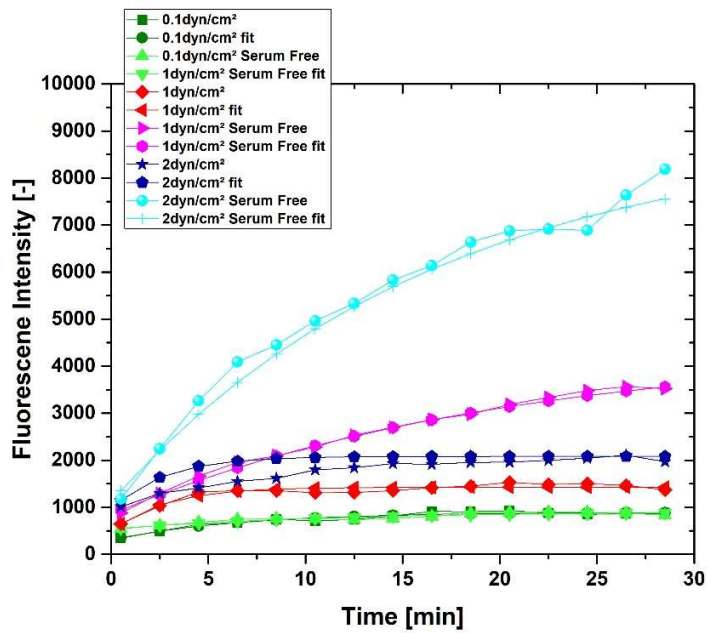
Figure 4.17: Averaged intensities with fitted curves over time in the adsorption phase with constant SWCNT concentration

The average correction value for this equation is $R^2 = 0.95$. Because of the two factors in the equation, A and R_0, both must be considered in combination to model the adsorption kinetics.

4.4.3   Desorption phase

With the intention of detecting a decrease in intensity, caused by desorption effects through washing, the following results are presented and discussed. In the first minute of washing, all desorption graphs in Figure 4.18, except for the constant graphs of low shear stress (0.1 dyn/cm²), show a decrease in intensity. The decreasing intensity was detected in the first 15-18 sec. of the washing phase. This decrease is the result of desorption of SWCNTs from the cells and the wash out of the suspended SWCNTs in the background of the fluorescence images. Particularly with regard to the used flow rates of medium and high shear stress, it results that the suspended SWCNTs are washed out after 2.8 seconds (1 dyn/cm²) or for high shear stress (2 dyn/cm²) after 1.4 seconds. Therefore, it is considered that the decrease in intensity shows desorption of SWCNTs. In the following 29.5 minutes of washing, the progression of the graphs is mostly constant, with fluctuation because of manually adjusted focus. Only the graph representing serum free media with shear stress of 1 dyn/cm² indicates ongoing desorption by continuous decreasing in intensity.
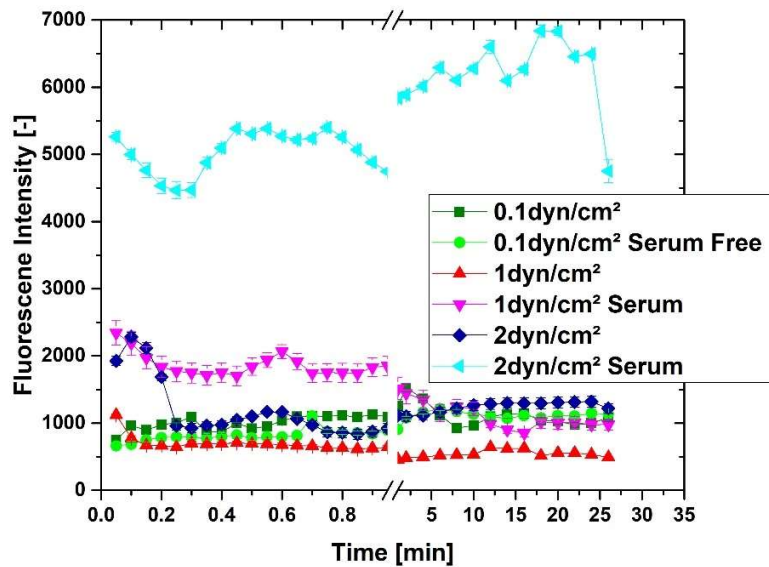
Figure 4.18: Intensity over time in the desorption phase with constant SWCNT concentration

In comparison to the adsorption ratios, the ratios in the desorption phase (see 6.12) are overall smaller than in the adsorption phase. The reason lies in the smaller intensity values at medium and high shear stress values, while the low shear stress intensities stayed relatively constant.

Table 4.4: Proportion of desorbed SWCNTs, considering adsorption with 100 %

	0.1 dyn/cm²		1 dyn/cm²		2 dyn/cm²	
	Media	**Serum Free**	**Media**	**Serum Free**	**Media**	**Serum Free**
Desorbed CNTs [%]	168	123	66	26	35	12
Uptaken CNTs [%]			33	74	65	88

To quantify the amount of desorbed SWCNTs, the overall average of each graph in desorption phase is calculated and compared with the corresponding averaged data in the adsorption phase (Table 4.4).

61

The resulting data for low shear stresses show a higher proportion of desorption than adsorption. This is not possible and indicates that the collected data at the lowest shear stress show fluctuations and no clear differences in between serum free and normal media. The signal intensity might also have not been high enough, caused by the low SWCNTs concentration or the overlapping signal from the background.

For medium shear stresses 2/3 and for high shear stresses about 1/3 of the absorbed SWCNTs were desorbed in media. This data show that a doubling of the shear stress (from 1 to 2 dyn/cm²) results in halving the amount of SWCNTs desorption. The same effect is also observed in absence of FBS (see Table 4.5). The serum free data show in detail, that in average about 1/4 of the SWCNTs are desorbed for conditions of medium shear stress, and only 1/8 at high shear stresses. Under the presence of FBS in the experiment, the amount of desorbed SWCNTs is in average 20 % higher than without extra proteins in the fluid.

Under the assumption of no SWCNT-transport out of the cell, the supplementary fraction represents the uptake by the cells. In general, SWCNTs showed under influence of FBS in average 32 % less uptake, than without FBS in serum free media. The doubling of shear stress leads to an increase of SWCNTs uptake by the cancer cells. At high shear stress (2 dyn/cm²), more (SF: 12%, M: 32%) SWCNTs were internalized than at medium shear stress (1 dyn/cm²).

Table 4.5: Overview of relative results in the mode of constant concentration in exp. phases

With respect to these numbers, it is possible to conclude, that without FBS in the dispersion, SWCNTs are 2.14x more likely to get internalized by the cells at higher shear stress of 2 dyn/cm² than at medium shear stress (1 dyn/cm²) under the described conditions (increase of 114 %).

Internalization and the binding studies were conducted at 37 °C. At this temperature, endocytosis is active which is supported by a moderate delivery of SWCNTs to the surface of the cells by medium flow rates. In the case that the shear stresses on the cells become too high (2 dyn/cm²) the endocytosis is inhibited and the internalization rate decreases. This effect is reflected in the discussed data and based on the limited binding energy and local SWCNT concentration on the cell membrane.

4.5 Static analysis

In this section evaluation without flow conditions are presented. The analysis of the static cell intensity images was conducted with the intention to verify the presented results of adsorption, desorption and uptake with cell images under flow. By examine the amount of SWCNTs before and after adsorption and desorption in the dispersion, an alternative method was applied. The following results show results based on flow conditions and static conditions with no shear stress (0 dyn/cm²).

4.5.1 Cell intensity analysis after adsorption and washing

The following analysis deals with the evaluation of the created hyperstack of fluorescent images. This hyperstack consists of images captioning the nIR intensity of cells at different spots in the flow chamber. These images were recorded after the adsorption phase of SWCNTs and secondly after the washing, in the uptake phase. Overall do the data in the mode of constant mass flux confirm the results in desorption phase. At least in term that the intensity values are all in the same range around the relative intensity value of 1000. An intensity decreasing between adsorption and uptake phase can be observed, due to washing. The bar chart Figure 4.19 indicates that more SWCNTs in serum free media are washed out than in normal media. At this point, the background has to be considered, which potentially has a bigger influence than in the flow channel, caused by a higher filling level.
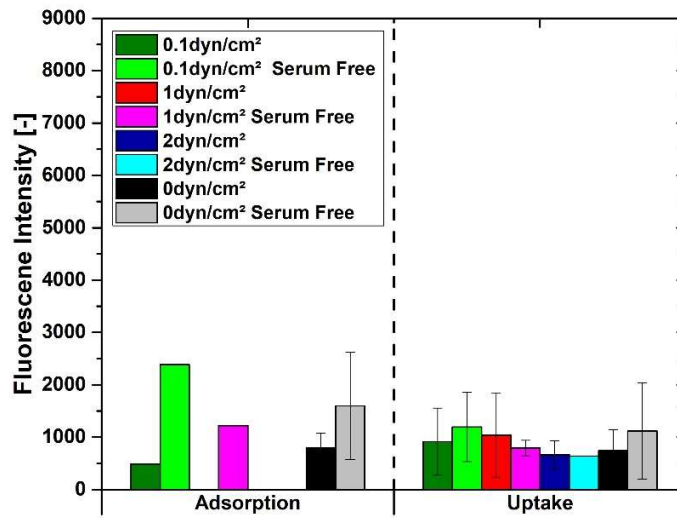
Figure 4.19: Intensities after CNTs adsorption and after washing (uptake) at const mass flux
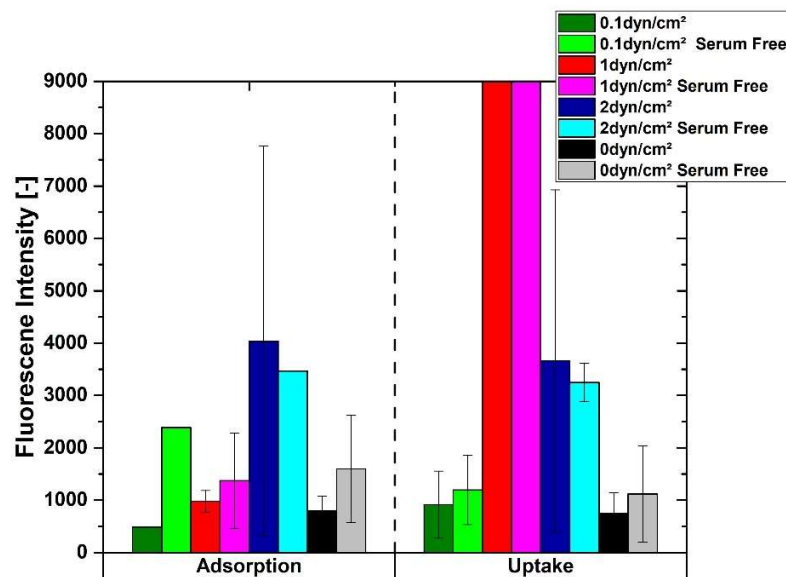
Figure 4.20: Intensities after CNTs adsorption and after washing (uptake) at const concentration

In addition to the results in the mode of constant concentration, there are higher intensity measured, like the measured results under flow (4.4). However, the detailed data of medium shear stress (1 dyn/cm²) and high shear stress (2 dyn/cm²) are not in agreement with the results under flow. In Figure 4.20, the results of 2 dyn/cm² do not

65

show higher intensities for the serum free dispersed SWCNTs, compared to media with FBS. The data of 1 dyn/cm² show in the adsorption phase significantly smaller intensity values and in the uptake phase untraceable high intensity values (see Figure 6.20) compared to flow conditions. These specific data are not expected from the recorded images since they should contain more reliable data because several spots with cells were recorded. The big differences are most likely due to problems in the step of applying the same threshold on every image of the hyperstack, which is documented in Figure 6.4.

4.5.2 Dispersion intensity analysis

In comparison to the previous intensity investigations of cells, the following results base on the concentration of the SWCNTs before and after the adsorption or washing procedure. In addition to the results in Figure 4.21, the cell coverage for each flow chamber must be considered, because the decrease of amount of SWCNTs after the adsorption as also the increase of SWCNTs by washing the cells with media, is directly related to the number of cells. The flow chambers 26-28 show all similar chamber coverage of 38 %. Therefore, the bar charts are representative and the relative decrease and increase in intensities, caused by the concentration of dispersed SWCNTs, are comparable. The applied statistics show the significance of the differences between the concentration before (initial) and after adsorption or desorption process. Considering the high statistical significance in Figure 4.21 it is being shown, that SWCNTs with in its used concentration are not an infinite source. Because of the lack of missing data and a variety of different experimental conditions the data are only rudimentarily

comparable. In terms of static vs. flow conditions, the data show that in media (#33), more SWCNTs are desorbed from the cells. Which is an indication for the effect, that cells in serum free media are internalizing a significant higher amount of SWCNTs (#31, #32).
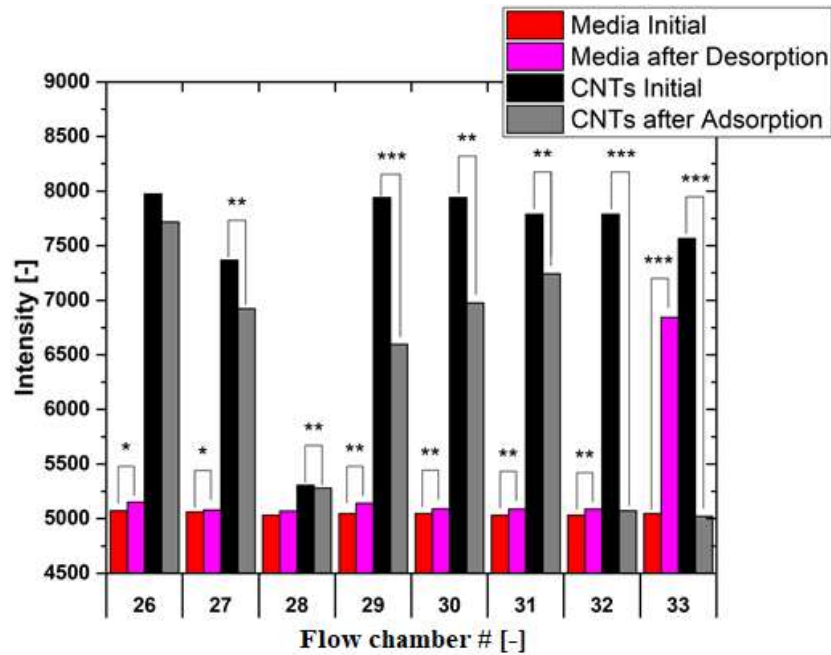
Figure 4.21: Intensity of dispersed SWCNTs under different experimental conditions

Table 4.6: List of experimental conditions in the dispersion analysis

Flow chamber #	Type of media	Shear stress [dyn/cm²]	SWCNTs Concentration [mg/L]	Comment	Statistics
26	M	2	0.9	Const. concentr.	$p < 0.05*$
27	SF	0.1	0.9	Const. mass flux	
28	SF	1	0.09	Const. mass flux	
29	M	1	0.9	Const. concentr.	$p < 0.01**$
30	M	1	0.9	Const. concentr.	
31	SF	0	0.9	Petri dish	
32	SF	0	0.9	Petri dish	$p < 0.001***$
33	M	0	0.9	Petri dish	

CHAPTER 5:   CONCLUSION

In this Master`s thesis, the influence of shear stress on the adsorption and desorption of single-walled carbon nanotube SWCNTs on lung cancer (A549) cells were studied using a microfluidic flow chamber and nIR hyperspectral microscopy. Therefore (1) the flow conditions and the A549 cells in the flow chamber and (2) the interactions between SWCNTs and A549 were quantified.

The velocity in the flow chamber was modeled by taking experimental data into account and comparing them to simulated velocities. The results of the experimental data demonstrated an influence of the Brownian motion and enabled the quantification of Brownian motion to an average velocity to 17 µm/sec in the flow chamber. The resulting Reynolds-numbers were determined to be Re $< 10^1$ and indicated stable laminar flow conditions throughout all applied flow rates.

Furthermore, all Peclet-numbers showed values higher than 1, which implied that the convection in the flow direction was more dominant than transversal diffusion transport of SWCNTs to the surface of the cells. An important verification for the comparability of the experiments is made by determining the average number of A549-cells to $1.2 \cdot 10^7$ ($\pm 0.25 \cdot 10^7$), which corresponds to average relative flow chamber coverage of 37.3 % (± 9.1 %).

Investigations with constant mass flux of SWCNTs have shown that at low shear stress (0.1 dyn/cm²) rates the SWCNTs were adsorbed and internalized more likely than under high shear stress (2 dyn/cm²). At high shear rates the forces applied by the flowing fluid must be larger than the binding forces, which prevents binding and detaches

bounded SWCNTs from the membrane. The effect of FBS, witch its main protein BSA, have not shown a clear influence on the rates of binding.

Investigations with a constant concentration in the dispersion lead, as expected, to higher SWCNT adsorption with increasing flow rate. The data of SWCNTs without FBS in the dispersion show an adsorption increase of 214 % by doubling the shear stress from 1dyn/cm² to 2 dyn/cm². SWCNTs under these conditions of lower protein level in the dispersion are more than two times (2.14x) more likely to get internalized by the cells This agrees and even exceeds the calculated predictions. In comparison, in the surroundings of FBS and more proteins in the suspension and high shear stresses of 2 dyn/cm² the probability of SWCNTs uptake is increased only by 35% in addition to medium shear stress. Under these conditions, SWCNTs were only 1.35x times more likely to get internalized by cells. Therefore, this last experimental setting with a higher variation of SWCNTs concentration shows that FBS inhibits the binding and uptake of SWCNTs under shear conditions. This is probably due to the formed protein corona of BSA proteins.

In terms of SWCNTs desorption from A549-cells, the experiments with a constant concentration found that for medium (1 dyn/cm²) shear stress 66 % and for high (2 dyn/cm²) shear stress 33 % of the absorbed SCWCNTs were desorbed in the presence of FBS. In addition to the serum free (no FBS) data, it is shown that in average only about 25 % of the SWCNTs are desorbed at conditions of medium shear stress, and only 12.5 % at high shear stress.

Furthermore, the collected data show that a doubling the shear stress (from 1 to 2 dyn/cm²) results in halving the amount of SWCNTs desorption, independent on the

influence of the protein level (with or without FBS). The presence of FBS leads to the conclusion, that the rate of desorbed SWCNTs is in average 20 % higher than without extra proteins (no FBS) in the fluid.

Concerning the uptake of SWCNTs, the results showed that under influence of FBS in average 32 % less uptake, than without FBS in serum free media. The doubling of shear stress leads to an increase of SWCNTs uptake by the cancer cells. At high shear stress (2 dyn/cm²), more (SF: 12%, M: 32%) SWCNTs were internalized than at medium shear stress (1 dyn/cm²).

Finally, it is to summarize that for *in vivo* applications the case of constant SWCNTs concentration in the blood media are more accurate and a possible future step. The investigations in this study predict, that SWCNTs will internalize higher rates into endothelia cells that are exposed to relatively high shear stresses. Despite this, the results concerning the shear stress independently of the SWCNT concentration showed, that the shear stress has only a marginal influence on the adsorption and desorption, compared to the impact that proteins binding to the surface create.

CHAPTER 6: APPENDICES

6.1 Experimental set-up:

Figure 6.1: Picture of the experimental set-up

6.2 Fluorescence Hyperspectral Microscope assembly:
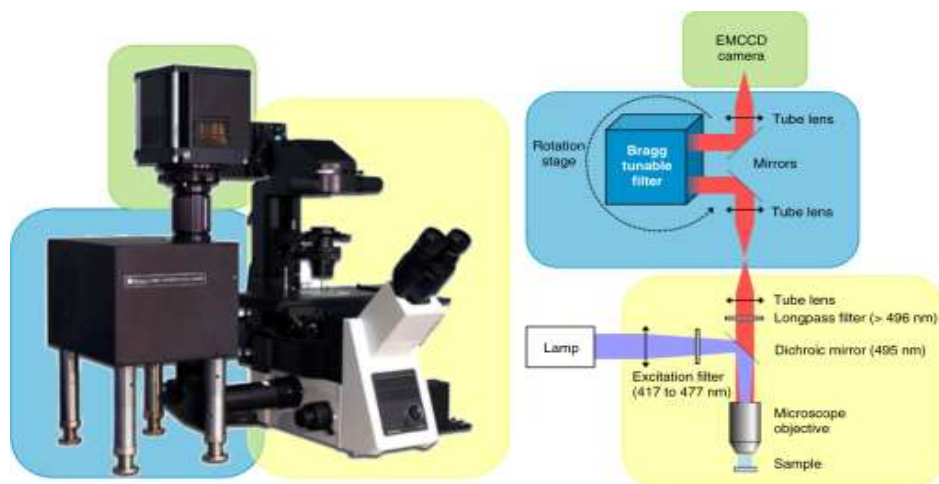
Figure 6.2: Acquisition system consisting consists of three main part: Creating inverted

microscope (yellow), BTF (blue), camera (green) [81].

6.3 NIR fluorescence hyperspectral microscope specifications

Near Infrared Hyperspectral Fluorescence Microscope (301 Morrill Hall): This state-of-the-art hyperspectral imaging system, manufactured by Photon Etc. (Montreal, Canada), uses a 2W 730 nm laser to spatially and spectrally image near-infrared emitting materials, namely single-walled carbon nanotubes, within live cells and organisms using an inverted Olympus IX-73 fluorescence microscope. A patented volume Bragg grating resolves fluorescence emission from each pixel of an imaging field between 900-1600 nm, and captures the image with a -80 °C thermo-electrically cooled 640×512 pixel InGaAs array near-infrared detector. Additionally, standard visible epifluorescence microscopy is enabled with an X-Cite mercury excitation source, filter cubes capable of imaging DAPI, FITC, Cy3, Cy5, ICG organic fluorophores, and co-planar CCD camera [82].

Table 6.1: Specification sheet of the NIR IMA™ Fluoresce Microscope

	IMA FLUORESCENCE VIS	IMA FLUORESCENCE IR
SPECTRAL RANGE	400 - 1000 nm	900 - 1700 nm
SPECTRAL RESOLUTION	< 2.5 nm	< 4 nm
LASER	OPTIONAL	808 nm
CAMERA	Front-illuminated interline CCD	InGaAs camera
EPIFLUORESCENCE FILTERS	Triple filter fluo	Optional
ILLUMINATION LAMP	HBO or XBO 100	Optional
DARKFIELD MODULE	Optional	Optional
OBJECTIVES	20x, 50x, 100x	20x, 60x, 100x
SPATIAL RESOLUTION	Sub-micron	
MICROSCOPE	Upright	
MAXIMUM SAMPLE FORMAT	4" x 4" (10 cm x 10 cm)	
X, Y TRAVEL RANGE	76 mm x 52 mm	
Z STAGE RESOLUTION	1 µm	
MAXIMUM SCANNING SPEED	150 ms	
WAVELENGTH ABSOLUTE ACCURACY	0.25 nm	0.5 nm
VIDEO MODE	Megapixel camera for sample visualisation	
PREPROCESSING	Spatial filtering, statistical tools, spectrum extraction, data normalization, spectral calibration	
HYPERSPECTRAL DATA FORMAT	FITS, HDF5	
SINGLE IMAGE DATA FORMAT	JPG, PNG, TIFF, CSV, PDF, SGV	
SOFTWARE	Computer with PHySpec™ control and analysis software included	
DIMENSIONS	≈ 40" x 30" x 30" (102 cm x 76 cm x 76 cm)	
WEIGHT	≈ 80 Kg	
*UPGRADES	IMA FLUORESCENCE VIS	IMA FLUORESCENCE IR
LASER	Additional excitation wavelengths available	
CAMERA HI	Back-illuminated camera	N/A
	EMCCD	N/A
HIGH-RESOLUTION MODULE	N/A	900-1700 nm, FWHM < 1 nm

6.4 Pump program:

In order to run the syringe pump with continuous flow and automatic withdrawing the pump program was filled with the following commands.

Table 6.2: Pump commands for continuous pumping with automatic withdrawing

Step	Command	Description
1	Rate	Rate: The Rate was set to the volumetric flow rate (0.11,1.06, 2.11 mL/min). Volume: The overall volume, which is pumped in this step was correspondent to the flow rate set to 0.11,1.06, 2.11 mL. (pumping direction: →)
2	Fill	Fill: This command was set to 0mL/min + with withdraw With this setting, the pump withdraws with the same rate at it pumped in the first command pumping direction: ←)
3	LP:EN	Loop: EN means Endless loop of steps 1,2

6.5 SWCNTs dispersion preparation:

Table 6.3: Dispersion preparation in dependent on the experimental mode

Mode	Settings:					
Const. Mass FLux-Fow Rates	Shear Stress τ [dyn/cm2]	vol. flow rate φ [μl/min]	c CNTs [mg/mL]	c CNTs [mg/L]	Suspension Vol. CNT [μL]	Sample Suspension Vol. Media [μL]
	0.1	110	0.000909	0.9091	22.2	4977.8
	1	1060	0.000094	0.0943	2.3 (4.6)	4997.7 (9995.4)
	2	2110	0.000047	0.0474	1.2 (2.4)	4998.8 (9997.6)
Inconstant Mass FLux-Flow Rates	Shear Stress τ [dyn/cm2]	vol. flow rate φ [μl/min]	c CNTs [mg/mL]	c CNTs [mg/L]	Suspension Vol. CNT [μL]	Sample Suspension Vol. Media [μL]
	0.1; 1;2	110,1060, 2110	0.000909	0.9091	22.2 (44.4)	4977.8 (9955.6)
	I With Intensity Study afterwards				51.06	11448.94
	II With Intensity Study afterwards				28.86	6471.14

6.6 Procedure: Cell splitting an inoculation of flow chamber

Sterile working regulations requires, that only sterilized equipment was used under the hood. Every item, which entered the hood was sterilized by using 70 % ethanol.

6.6.1 Cell splitting

1. Suck old Media Dulbecco's Modified Eagle Medium-DMEM(gibco®) out of the flask.

2. Rinsing with 2 mL of Phosphate Buffered Saline PBS pH 7.4 (gibco®)-sucking it out.

3. Detach the cells from the bottom of the flask with 2 mL of Trypsin-TrypLE™ Express (gibco®)-let it sit in the incubator for 5 min.

4. Take 3500 µL cell-suspension on 20 mL of media in a new 75 cm³ tissue culture flask (Celltreat®)-Incubator

5. Splitting end

6.6.2 Inoculate flow chamber

6. Pipette Mixing – 50 µL for the cell counting in the cellometer.

7. Prepare dispersion of cell-medium in a concentration of $2 \cdot 10^6$ cells/mL (at least 0.5 mL of cells)

8. Control the concentration of the suspension with the cell-counter and write it down (Cellometer Mini (Nexcolom Bioscience®)

9. Fill 100 µL of the prepared cell dispersion in the flow chamber

10. Fill afterwards 60 µL Media in each reservoir-close them with caps

11. Incube them for 2days (48 h)

6.6.3 Composition of complete- and serum free media

Table 6.4: Composition of media and serum free media

Components	Volume [mL]	Complete media (M)	Serum free media (SF)
DMEM	500	x	x
Penicilline	5	x	x
L-Glutamin*	145.6	x	x
Anti Fungi	1	x	x
HEPES*	12.5	x	x
FBS*	50	x	-

*Fetal Bovine Serum (FBS)

FBS contains hormones, paracrine, endocrine and autocrine growth factors and rich variety of proteins which support cell growth 49. The details composition of FBS is listed in

Table **6.5**. Even more detailed composition of FBS is published by Lindl et al [83].

Table 6.5: Composition of FBS [84,85]

Composition of Fetal Bovine Serum		
Components	Conc.	Range
total protein	3.8 g/100 ml	3.2 - 7.0
albumin	2.3 g/100 ml	2.0 - 3.6
endotoxin	0.36 ng/ml	0.01 - 10.0
haemoglobin	11.3 mg/100 ml	2.4 - 18.1
cholesterol	31 mg/100 ml	12 - 63
fatty acids phospholipids triglycerides	mg/ml	
glucose	125 mg/100 ml	85 - 247
insulin	10 µU/ml	6 - 14
cortisone	0.5 µg/100 ml	<0.1 - 2.3
trijodo-thyronine	119 ng/100 ml	56 - 223
thyroxine	12.1 ng/100 ml	7.8 - 15.6
PTH	1718 pg/ml	85 - 6180
PGE	5.91 ng/ml	0.5 - 30.5
PGF	12.33 ng/ml	3.8 - 42.0

The origin and function of the mentioned growth hormones are explained briefly in the following paragraph. These hormones are produced by Autocrine and Paracrine and are restricted to work within the cytoplasm of the cell where exocrine and endocrine hormones move to within the organism.

- Autocrine: Hormones that act on the same cell that produced them

- Paracrine: Local hormones which diffuse a short distance to other cells.

- Endocrine: Hormones, secreted into the blood and have a wide acting range

- Exocrine: Non-hormone secretion into ducts

Physical properties of BSA:

- Number of amino acid residues: 583
- Molecular weight: 66,463 Da (= 66.5 kDa)
- isoelectric point in water at 25 °C: 4.7[1]
- Extinction coefficient of 43,824 M^{-1}cm^{-1} at 279 nm[2]
- Dimensions: $140 \times 40 \times 40$ Å (prolate ellipsoid where a = b < c)[3]
- pH of 1% Solution: 5.2-7 [4][5]
- Optical Rotation: $[\alpha]259$: -61°; $[\alpha]264$: -63°[4][5]
- Stokes Radius (r_s): 3.48 nm[6]
- Sedimentation constant, $S_{20,W} \times 10^{13}$: 4.5 (monomer), 6.7 (dimer)[4][5]
- Diffusion constant, $D_{20,W} \times 10^{-7}$ cm2/s: 5.9[4][5]
- Partial specific volume, V_{20}: 0.733[4][5]
- Intrinsic viscosity, η: 0.0413[4][5]
- Frictional ratio, f/f0: 1.30[4][5]
- Refractive index increment (578 nm) $\times 10^{-3}$: 1.90[4][5]
- Optical absorbance, A279 nm1 g/L: 0.667[4][5]
- Mean residue rotation, [m']233: 8443[4][5]
- Mean residue ellipticity: 21.1 $[\theta]209$ nm; 20.1 $[\theta]222$ nm[4][5]
- Estimated a-helix, %: 54[4][5]
- Estimated b-form, %: 18[4][5]
  [1]-[86]
  [2]-[87]
  [3]-[88]
  [4]-[89]
  [5]-[90]
  [6]-[91]

*L-Glutamin:

L-glutamine is an unstable (strongly pH-dependent) essential amino acid required in cell culture media formulations. As an growth factor, it enhances the growth of cells, with high energy demands [92].

*HEPES:

(4-(2-hydroxyethyl)-1-piperazineethanesulfonic acid) is a zwitterionic organic chemical buffering agent and is categorized as a "Good" buffer which derives from a set of buffers described by Dr. Norman Good and his colleagues in 1966 [93,94].

6.6.4 Cell culture equipment

1. <u>Eppendorf New Brunswick Galaxy 170 S Incubator:</u>

This 170 L cell culture incubator features a 4-port sealed inner glass door, IR CO_2 sensor, high temperature sterilization, RS-232 communication port, 25 mm access ports [82], used with 5% N_2.

2. <u>Liquid Nitrogen Storage System (301 Morrill Hall):</u>

This large liquid nitrogen cryo-vessel is capable of storing thousands of cryogenically preserved cell samples and constantly monitors liquid nitrogen levels to maintain the viability of these samples.
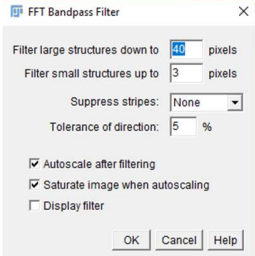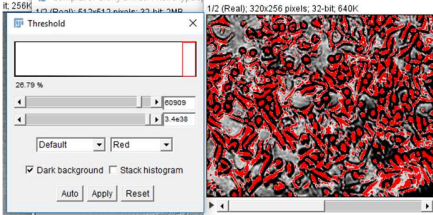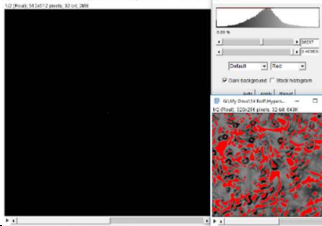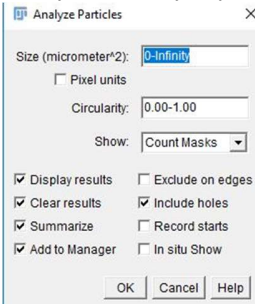
3. <u>Labconco Purifier Logic+ Class II, Type A2 Biosafety Cabinet (301 Morrill Hall):</u>

This brand new 4 foot standard bio-safety cabinet features a 10″ sash opening, UV light, service fixture, vacu-pass portal, and base stand.

6.7 ImageJ evaluation procedures:

6.7.1 Cell coverage

Table 6.6: Procedure of cell coverage analyses

Step	Command	Program path and description
1	Load HDF5 Correct	Load Picture → 8 bit Ctrl+C – Auto
2	Enhance contrast	x Process-Enhanced Contrast saturated pixels 0.3% normalize
3	Process FFT bandpass filter Threshold Use Fourier Transformation for threshold	
4	Analyze particles	Analyze – Analyze particles
5	Save as	Save Summary and Results Table with the Label Name (Sample Name)
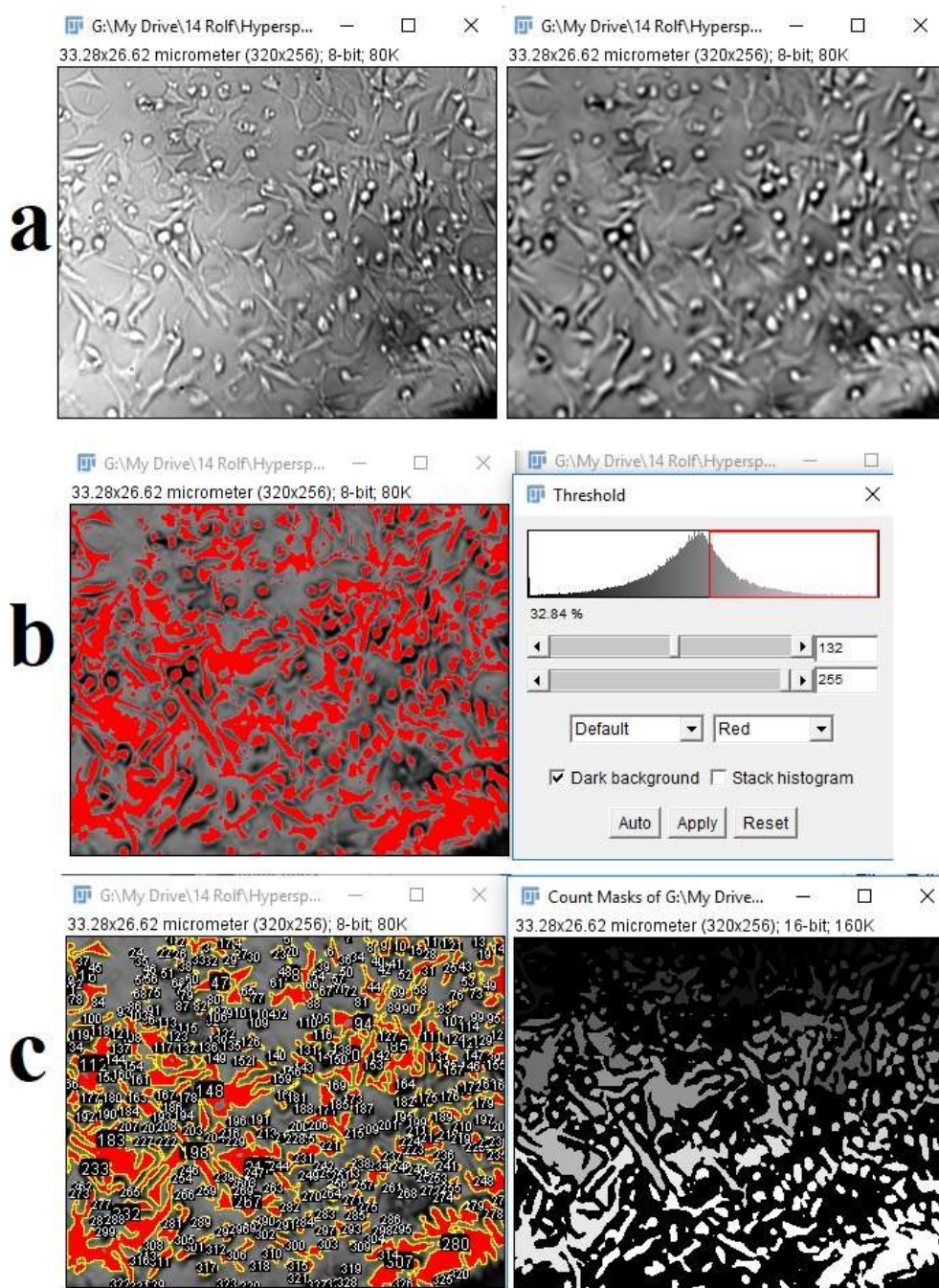
Figure 6.3: Coverage evaluation of flow chamber #5 (20x, 0.02s exp. Time). (a) left: Image converted into 8-bit format, B&W constrast allplied, contrast applied, right: FFT Bandpass filter applied; (b) manual threshold applied; (c) left: Count masks, right: Outline mask

6.7.2 **Hyperstack**

The hyperstack consists stacks made of 5-images each. These stacks were recorded after the adsorption phase and after the washing, focusing the uptake of the cells. With the high number of pictures and a lot of different settings, the intensities turned out very different from each other. This fact impeded the evaluation of the super stack with the threshold as showed below. There were two evaluation ways proposed. One with 32-bit and one with 8-bit images. The two evaluation procedures are due to locations with very high intensity values (mean = 55515) for untreated 32-bit images.

Figure 6.4: Applying threshold on images (32-bit images) in the hyperstack with untraceable high intensity values and resulting step sizes for adjusting the threshold

These intensities are based on white dots with high intensities (see Figure 6.5), which were present even though the images were background subtracted.
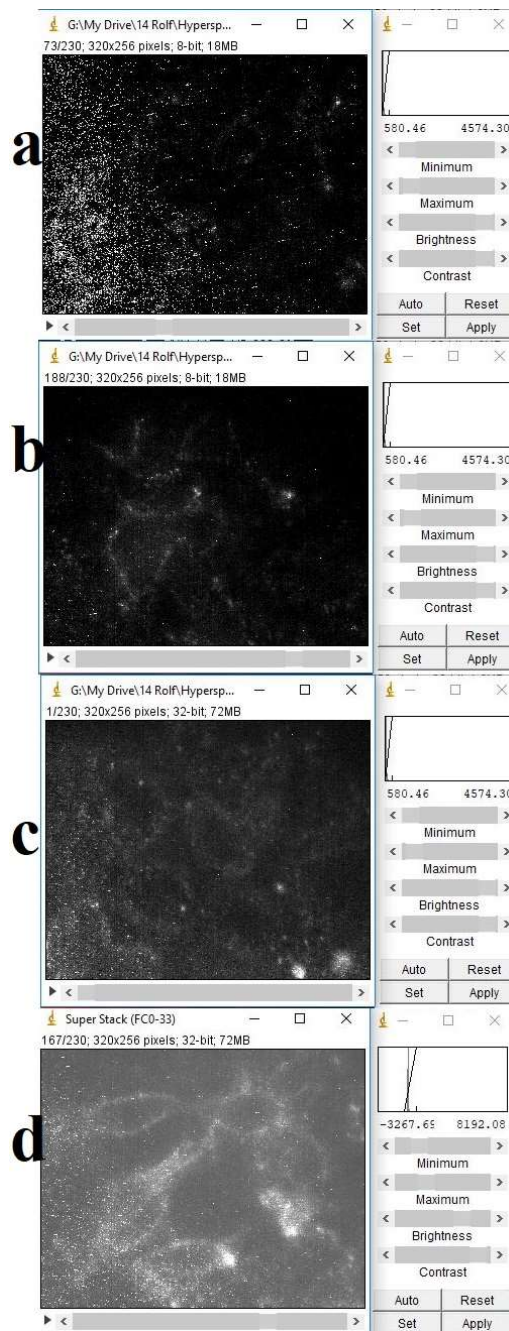
Figure 6.5: Applied black and white contrast (B&W) of images of the hyperstack. (a): Image showing dots with high intensities, which were observed over several other stacks; (b) image with medium B&W contrast; (c) image with high medium B&W contrast; (d) image with changed B&W contrast range, showing contrast of cells to the background.

To filter these out the threshold was set (32-bit procedure) or the images were treated with contrast enhancement and format shifting (8-bit procedure).
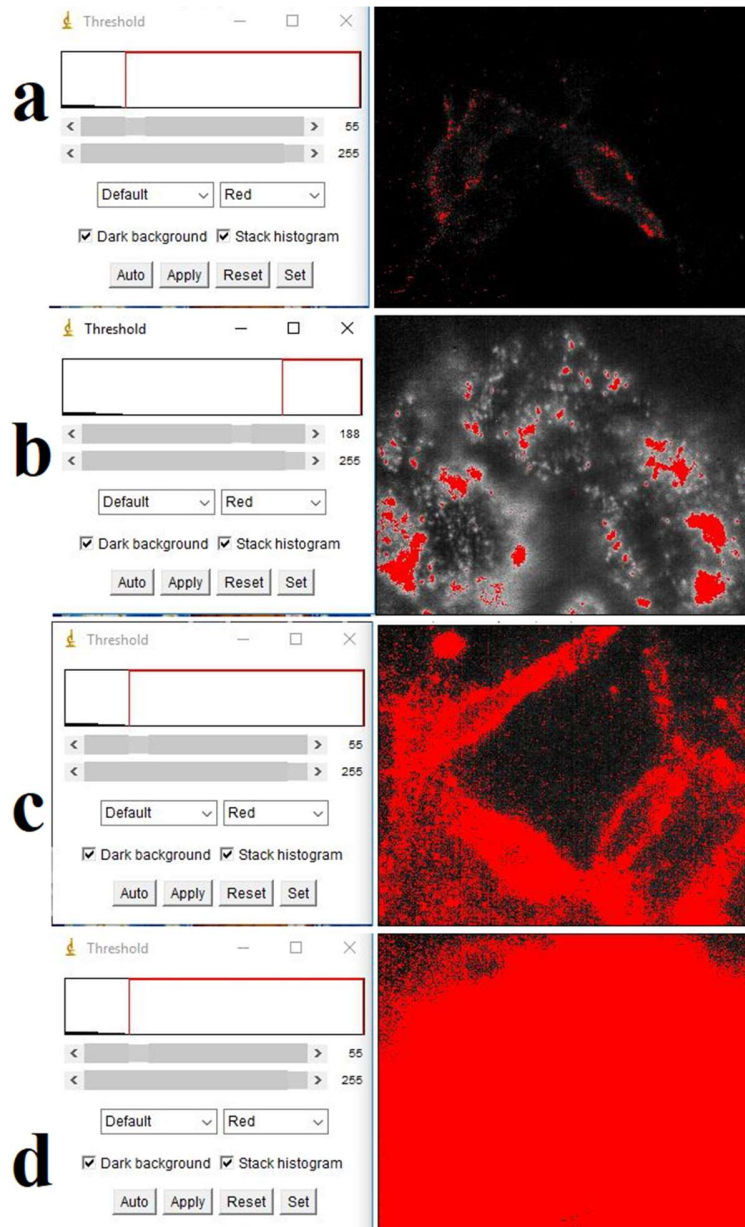
Figure 6.6: Evaluation procedure of the hyperstack with treated 8-bit images.(a): Image with low intensity by SWCNTs and wide range threshold; (b) Image with a different higher and smaller threshold range shows only high intensity locations; (c) Image with medium intensity by SWCNTs and wide range threshold; (d) Image with high intensity by SWCNTs and wide range threshold.

6.7.3 Focusing

In this section, merged images consistent of WL and nIR images are shown.

These images illustrate the possibility of variable focusing in the experiments.
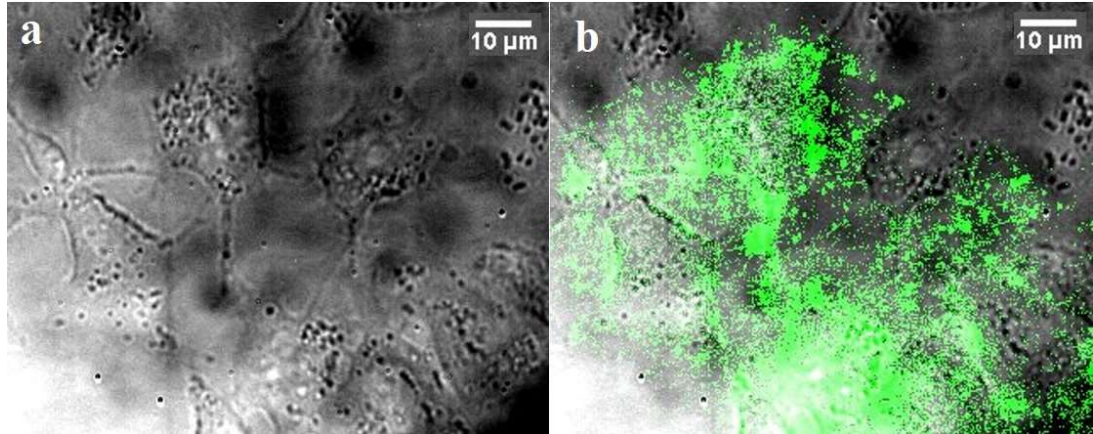
Figure 6.7: Focused on the bottom surface of the flow chamber (a) A549 cells (b) merged with SWCNT channel after 30min exposure (FC28)
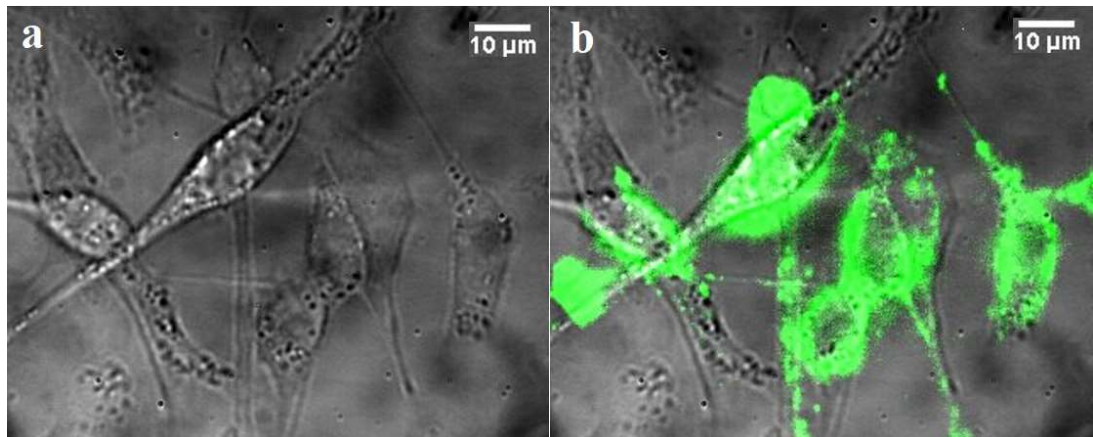
Figure 6.8: Focused (a) A549 cells (b) merged with SWCNT channel after 30min exposure (FC28)

6.8 Table of shear stress:

Table 6.7: Shear Stress Values for the used Flow Chamber

Shear Stress table for µ-Slide I $^{0.4}$ Luer for viscosity η=0.0072 dyn·s/cm²:

τ [dyn/cm²]	Φ [ml/min]	τ [dyn/cm²]	Φ [ml/min]	τ [dyn/cm²]	Φ [ml/min]
0.1	0.11	3.5	3.69	25	26.38
0.2	0.21	4	4.22	30	31.66
0.3	0.32	4.5	4.75	35	36.94
0.4	0.42	5	5.28	40	42.22
0.5	0.53	5.5	5.80	45	47.49
0.6	0.63	6	6.33	50	52.77
0.7	0.74	7	7.39	55	58.05
0.8	0.84	8	8.44	60	63.32
0.9	0.95	9	9.50	65	68.60
1	1.06	10	10.55	70	73.88
1.2	1.27	11	11.61	75	79.15
1.4	1.48	12	12.66	80	84.43
1.6	1.69	13	13.72	85	89.71
1.8	1.90	14	14.78	90	94.98
2	2.11	15	15.83	95	100.26
2.2	2.32	16	16.89	100	105.54
2.4	2.53	18	19.00	105	110.82
2.6	2.74	20	21.11	110	116.09
2.8	2.96	22	23.22	115	121.37
3	3.17	24	25.33	120	126.65

$$\tau \left[\frac{dyn}{cm^2}\right] = \eta \left[\frac{dyn \cdot s}{cm^2}\right] \cdot 131.6 \cdot \Phi \left[\frac{ml}{min}\right]$$

☐ = used shear values
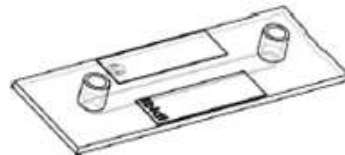
6.9 Velocity characterization:
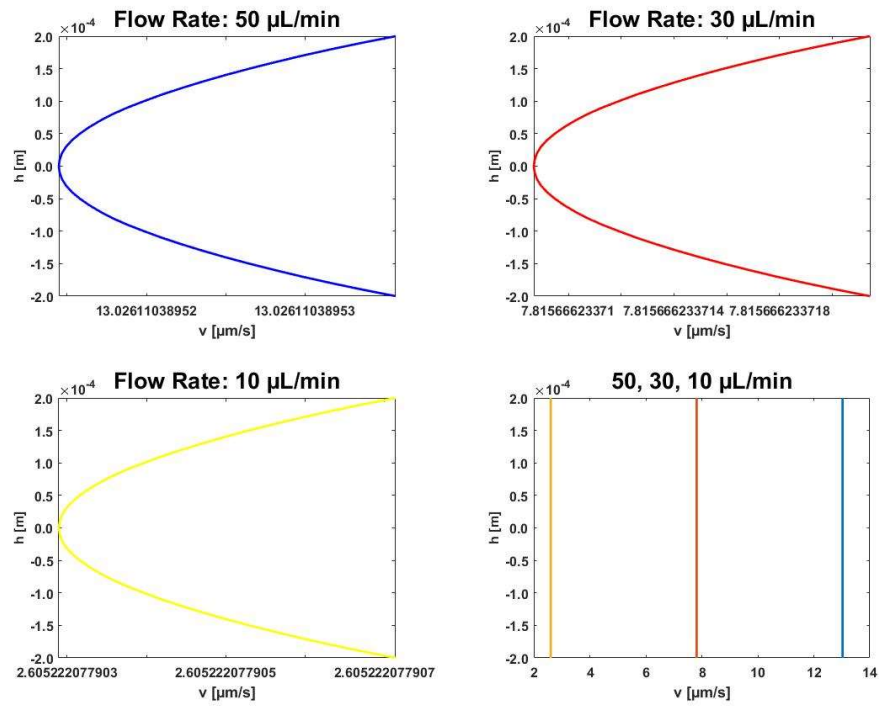
Figure 6.9: Simulated velocity profiles based on equation of [57] in central point of the flow chamber dependent on flow rates between 2 and 50 µL/min.
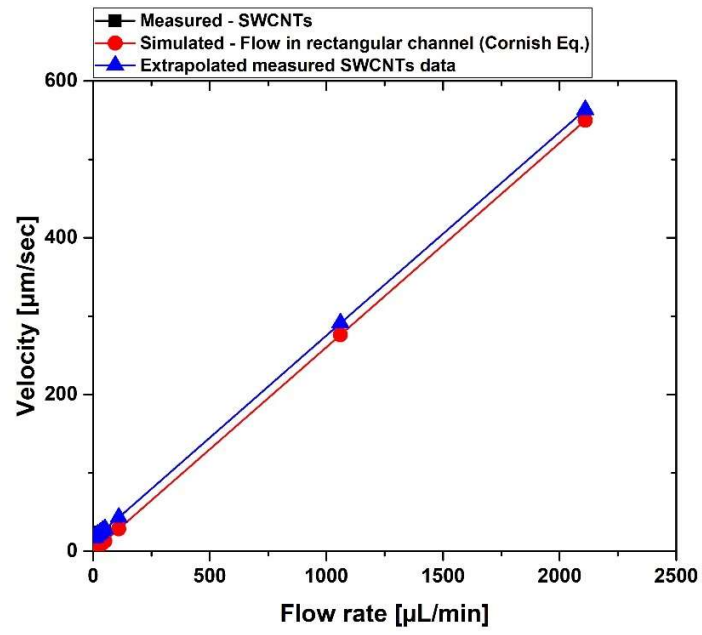
Figure 6.10: Comparison of all simulated, measured and linear extrapolated velocities

6.10 Cell intensity graphs:
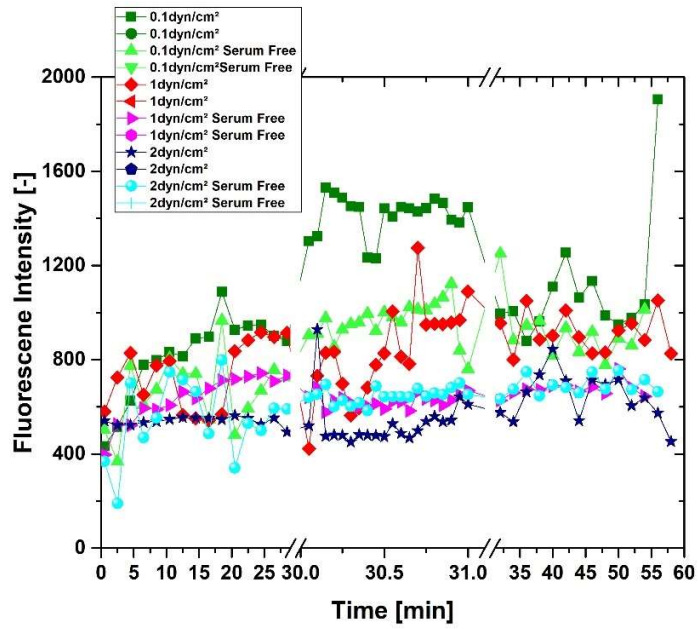
Figure 6.11: Recorded intensity over time trough 3 experimental phases of constant mass flux
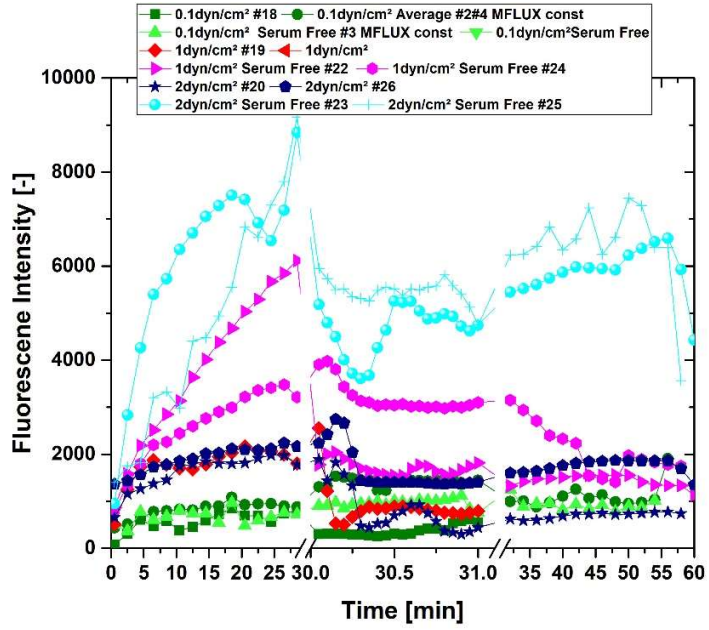
Figure 6.12: Recorded intensity over time trough 3 experimental phases of constant concentration
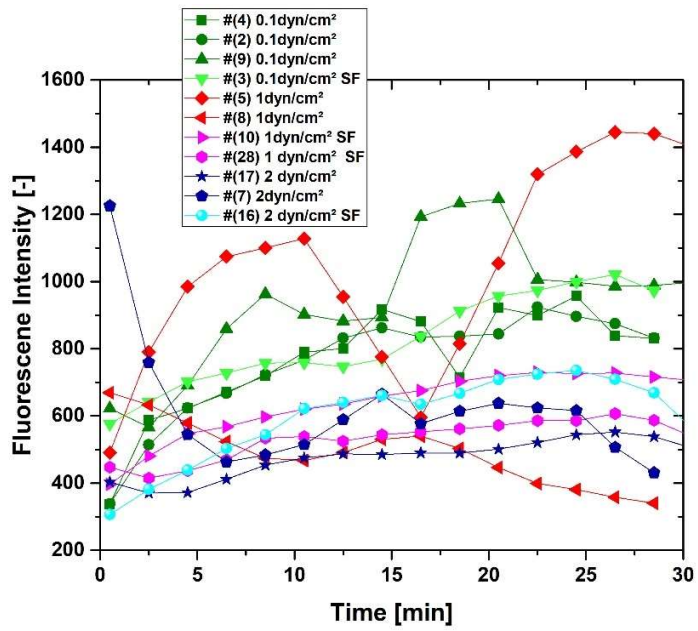
Figure 6.13: All Intensity data over time in the adsorption phase with const. SWCNT mass flux
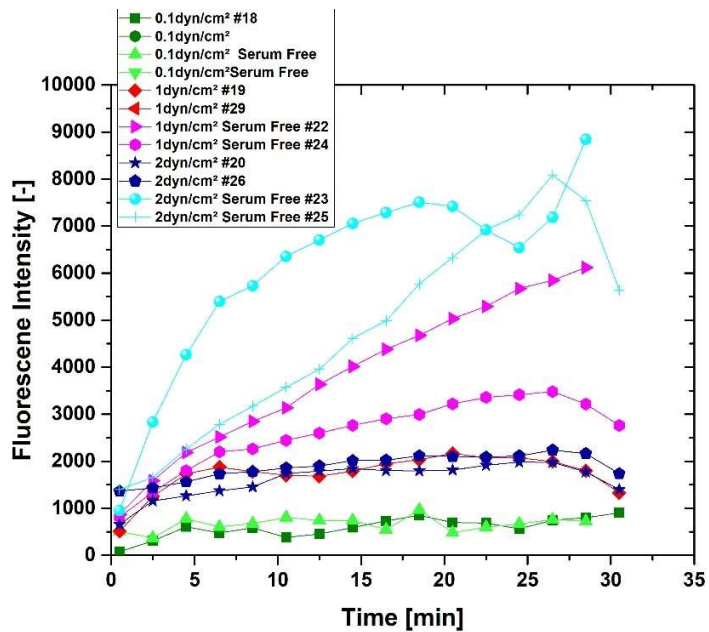
Figure 6.14: All Intensity data over time in adsorption phase with const. SWCNT concentration
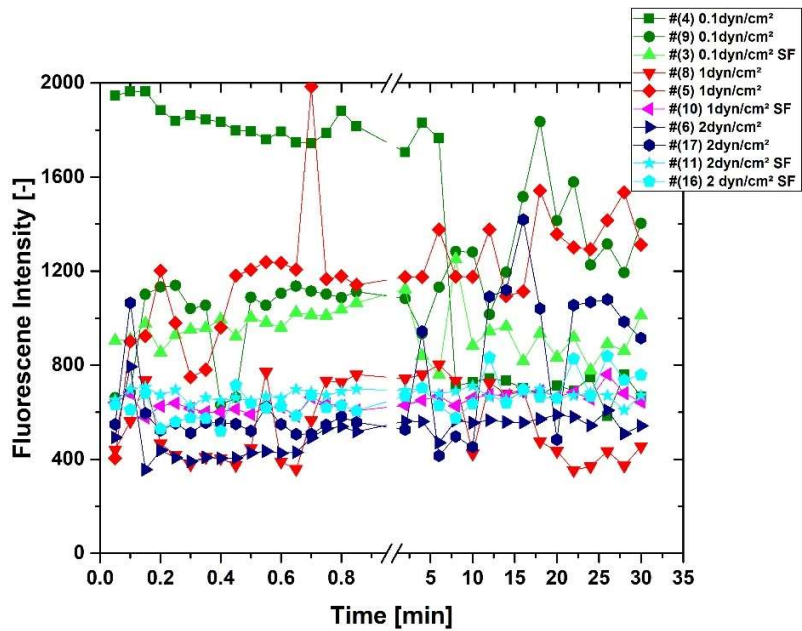
Figure 6.15: All Intensity data over time in desorption phase with const. SWCNT mass flux
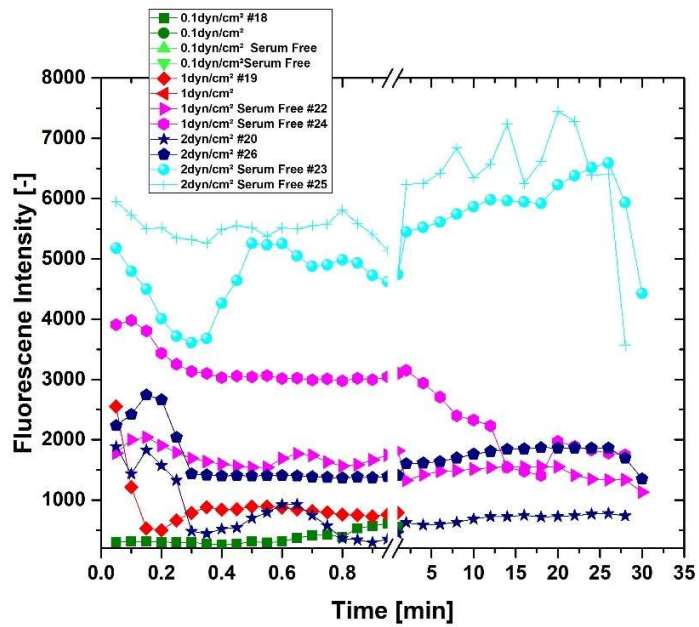
Figure 6.16: All Intensity data over time in desorption phase with const. SWCNT concentration

6.11 Peclet-number (Pe):
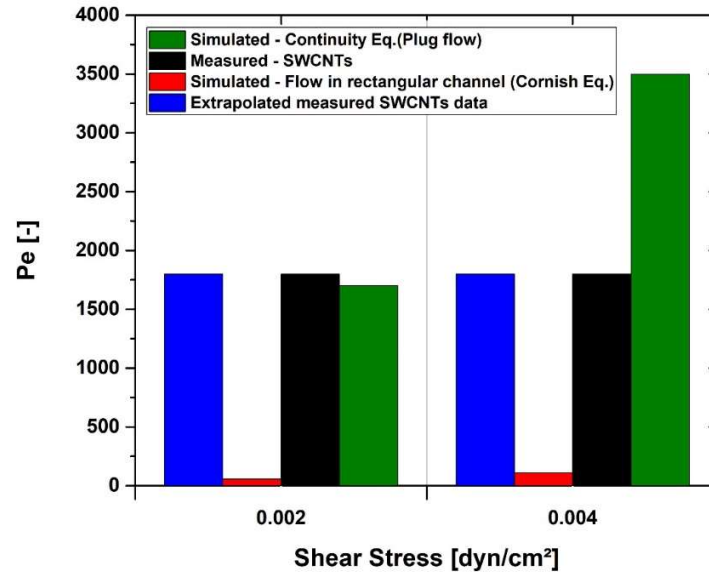
Figure 6.17: Peclet number over shear stress resulting from the lowest flow rates 2 and 4 µL/min
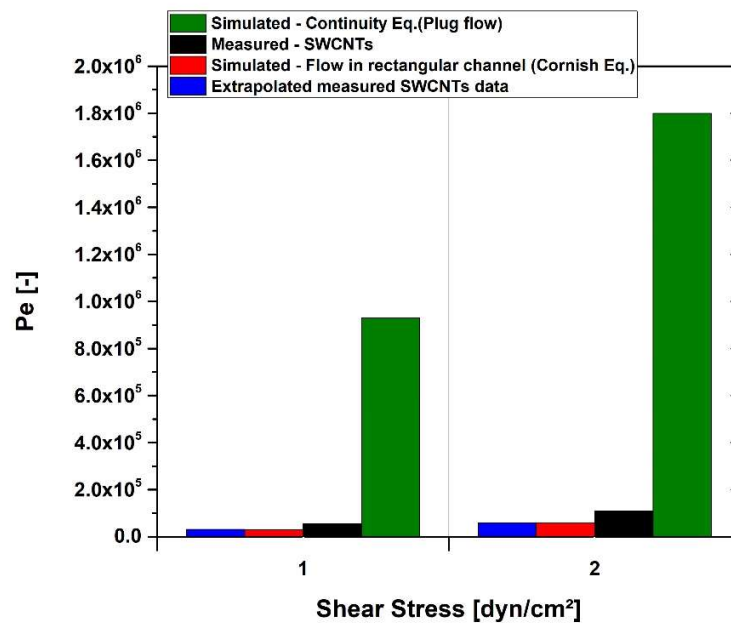
Figure 6.18: Pe over shear stress resulting from the highest flow rates 1060 and 2110 µL/min

6.12 Averaged cell intensity tables:

Table 6.8: Ratios [-] of averaged adsorption intensities with regard to values of 0.1 dyn/cm²

Shear stress ratio	$\dfrac{1\ \text{dyn/cm}^2}{0.1\ \text{dyn/cm}^2}$	$\dfrac{2\ \text{dyn/cm}^2}{0.1\ \text{dyn/cm}^2}$
Factor of increased mass flux	**10**	**20**
M-Media (with FBS)	1.7	2.3
SF-Serum free media (no FBS)	3.3	7.0
SF / M	1.9	3.1

Table 6.9: Ratios [-] of averaged desorption (1st min) intensities regarding values of 0.1 dyn/cm²

Shear stress ratio	$\dfrac{1\ \text{dyn/cm}^2}{0.1\ \text{dyn/cm}^2}$	$\dfrac{2\ \text{dyn/cm}^2}{0.1\ \text{dyn/cm}^2}$
Factor of increased mass flux	**10**	**20**
M-Media (with FBS)	0.8	1
SF-Serum free media (no FBS)	2.3	6.3
SF / M	3.1	5.7

Table 6.10: Ratios [-] of averaged desorption (2-30 min) intensities regarding values of 0.1 dyn/cm²

| Shear stress ratio	$\dfrac{1\ \text{dyn/cm}^2}{0.1\ \text{dyn/cm}^2}$	$\dfrac{2\ \text{dyn/cm}^2}{0.1\ \text{dyn/cm}^2}$
Factor of increased mass flux	**10**	**20**
M-Media (with FBS)	0.5	1.1
SF-Serum free media (no FBS)	1.0	5.5
SF / M	2.1	5.0

Table 6.11: Ratios [-] of averaged desorption (0-30 min) intensities regarding values of 0.1 dyn/cm²

Shear stress ratio	$\dfrac{1\ \text{dyn/cm}^2}{0.1\ \text{dyn/cm}^2}$	$\dfrac{2\ \text{dyn/cm}^2}{0.1\ \text{dyn/cm}^2}$
Factor of increased mass flux	**10**	**20**
M-Media (with FBS)	0.5	0.7
SF-Serum free media (no FBS)	0.7	0.7
SF / M	1.5	1.0

6.13 Cell intensity analysis after adsorption and washing:
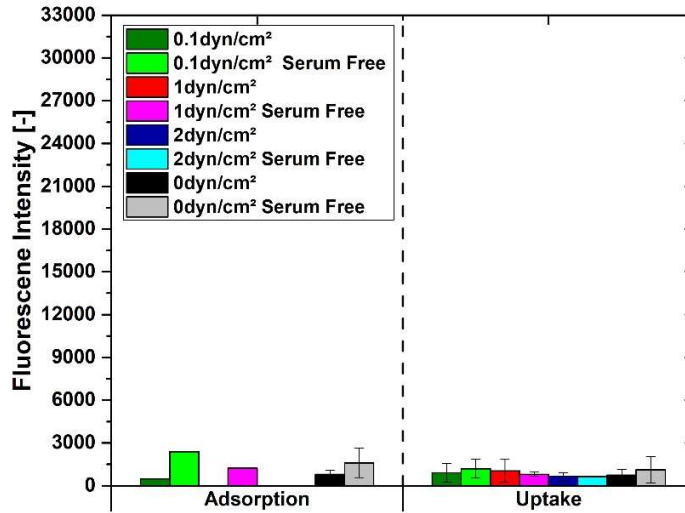
Figure 6.19: Intensities after CNTs adsorption and after washing (uptake) at const mass flux
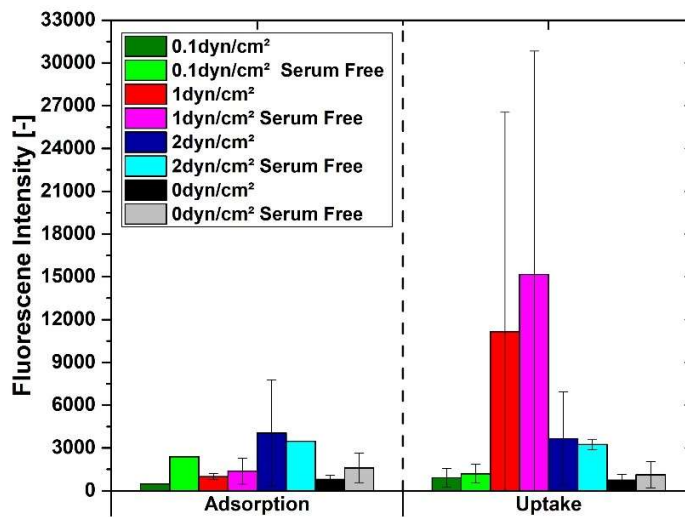
Figure 6.20: Intensities after CNTs adsorption and after washing (uptake) at const concentration

6.14 Dispersion intensity analysis:
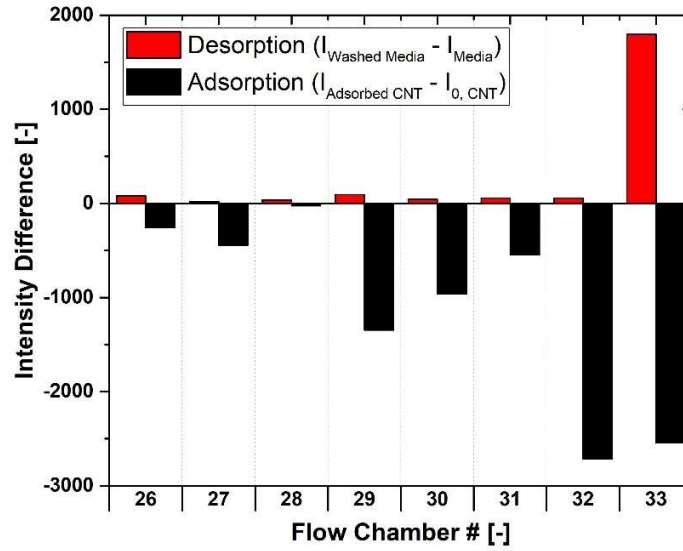
Figure 6.21: Comparison of the differences between the amount of adsorbed and desorbed proportion of SWCNTs
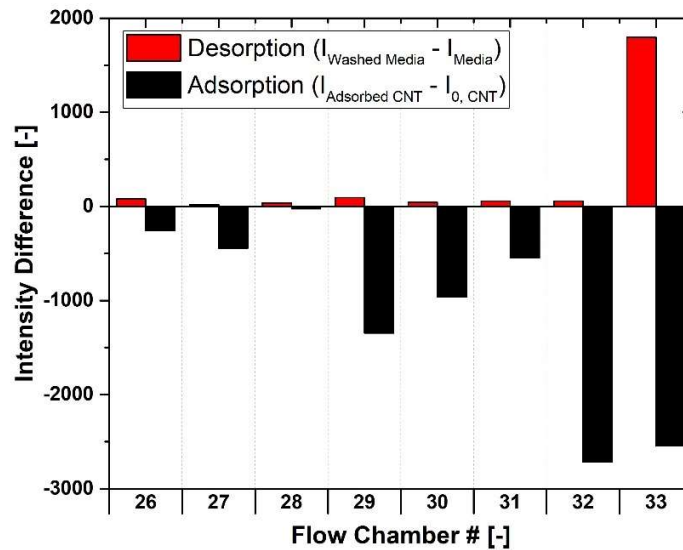
Figure 6.22: Comparison of the ratios between the amount of *adsorbed* and *desorbed* proportion of SWCNTs

6.15 Zeta Potential:
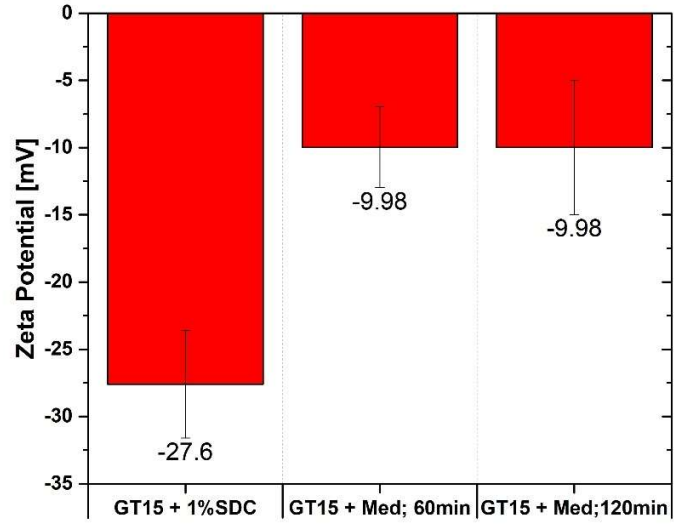
Figure 6.23: Zeta potential of SWCNTs in SDC or Media (Med) under static conditions

BIBLIOGRAPHY

(1)   Jin, H.; Heller, D. A.; Sharma, R.; Strano, M. S. Size-Dependent Cellular

Uptake and Expulsion of Single-Walled Carbon Nanotubes: Single Particle

Tracking and a Generic Uptake Model for Nanoparticles. *ACS Nano* **2009**, *3*

(1), 149–158.

(2)   Jena, P. V.; Safaee, M. M.; Heller, D. A.; Roxbury, D. DNA–Carbon Nanotube

Complexation Affinity and Photoluminescence Modulation Are Independent.

ACS Appl. Mater. Interfaces **2017**, *9* (25), 21397–21405.

(3)   Wang, X.; Li, Q.; Xie, J.; Jin, Z.; Wang, J.; Li, Y.; Jiang, K.; Fan, S. Fabrication

of Ultralong and Electrically Uniform Single-Walled Carbon Nanotubes on

Clean Substrates. *Nano Lett.* **2009**, *9* (9), 3137–3141.

(4)   Budhathoki-Uprety, J.; Langenbacher, R. E.; Jena, P. V.; Roxbury, D.; Heller,

D. A. A Carbon Nanotube Optical Sensor Reports Nuclear Entry via a

Noncanonical Pathway. *ACS Nano* **2017**, *11* (4), 3875–3882.

(5)   Harvey, J. D.; Baker, H. A.; Mercer, E.; Budhathoki-Uprety, J.; Heller, D. A.

Control of Carbon Nanotube Solvatochromic Response to Chemotherapeutic

Agents. *ACS Appl. Mater. Interfaces* **2017**, *9* (43), 37947–37953.

(6)   Schroeder, A.; Winslow, M. M.; Anderson, D. G.; Heller, D. A. Treating

metastatic cancer with nanotechnology

https://www.researchgate.net/publication/51919618_Treating_metastatic_cance

r_with_nanotechnology (accessed Jun 13, 2018).

(7)   Lingjie, M.; Xiaoke, Z.; Qinghua, L.; Zhaofu, F.; Paul J., D. Single walled

        carbon nanotubes as drug delivery vehicles: Targeting doxorubicin to tumors -

        ScienceDirect

        https://www.sciencedirect.com/science/article/pii/S0142961211013421?via%3

        Dihub (accessed Jun 13, 2018).

(8)   Hong, G.; Diao, S.; Antaris, A. L.; Dai, H. Carbon Nanomaterials for Biological

        Imaging and Nanomedicinal Therapy - Chemical Reviews (ACS Publications)

        https://pubs.acs.org/doi/10.1021/acs.chemrev.5b00008 (accessed Jun 13, 2018).

(9)   Boghossian Ardemis A.; Zhang Jingqing; Barone Paul W.; Reuel Nigel F.;

        Kim Jong-Ho; Heller Daniel A.; Ahn Jin-Ho; Hilmer Andrew J.; Rwei Alina;

        Arkalgud Jyoti R.; et al. Near-Infrared Fluorescent Sensors Based on Single-

        Walled Carbon Nanotubes for Life Sciences Applications. *ChemSusChem* **2011**,

        4 (7), 848–863.

(10)   Sambale, F.; Stahl, F.; Bahnemann, D.; Scheper, T. In Vitro Toxicological

        Nanoparticle Studies under Flow Exposure. *J. Nanoparticle Res.* **2015**, *17* (7),

        298.

(11)   Jurney, P.; Agarwal, R.; Roy, K.; Sreenivasan, S. V.; Shi, L. Size-Dependent

        Nanoparticle Uptake by Endothelial Cells in a Capillary Flow System. *J.

        Nanotechnol. Eng. Med.* **2015**, *6* (1), 011007-011007–6.

(12)   Samuel, S. P.; Jain, N.; O'Dowd, F.; Paul, T.; Kashanin, D.; Gerard, V. A.;

        Gun'ko, Y. K.; Prina-Mello, A.; Volkov, Y. Multifactorial Determinants That

Govern Nanoparticle Uptake by Human Endothelial Cells under Flow. *Int. J. Nanomedicine* **2012**, *7*, 2943–2956.

(13)   Farokhzad, O. C.; Langer, R. Impact of Nanotechnology on Drug Delivery. *Acs Nano* **2009**, *3* (1), 16–20.

(14)   Mitchell, M. J.; King, M. R. Computational and Experimental Models of Cancer Cell Response to Fluid Shear Stress. *Front. Oncol.* **2013**, *3*.

(15)   Polacheck, W. J.; Charest, J. L.; Kamm, R. D. Interstitial Flow Influences Direction of Tumor Cell Migration through Competing Mechanisms. *Proc. Natl. Acad. Sci. U. S. A.* **2011**, *108* (27), 11115–11120.

(16)   Han, J.; Shuvaev, V. V.; Davies, P. F.; Eckmann, D. M.; Muro, S.; Muzykantov, V. R. Flow Shear Stress Differentially Regulates Endothelial Uptake of Nanocarriers Targeted to Distinct Epitopes of PECAM-1. *J. Control. Release Off. J. Control. Release Soc.* **2015**, *210*, 39–47.

(17)   Lin, A.; Sabnis, A.; Kona, S.; Nattama, S.; Patel, H.; Dong, J.-F.; Nguyen, K. T. Shear-Regulated Uptake of Nanoparticles by Endothelial Cells and Development of Endothelial-Targeting Nanoparticles. *J. Biomed. Mater. Res. A* **2010**, *93A* (3), 833–842.

(18)   Karimi, M.; Ghasemi, A.; Mirkiani, S.; Moosavi, S. M.; Moosavi Basri, S. M.; Hamblin, M. R. *Carbon Nanotubes in Drug and Gene Delivery*; IOP Publishing, 2017.

(19)   Zhang, W. Saliva and Breath Based Biosensing System for Disease Detection and Monitoring. **2016**, 166.

(20)   O'Connell, M. J.; Bachilo, S. M.; Huffman, C. B.; Moore, V. C.; Strano, M. S.; Haroz, E. H.; Rialon, K. L.; Boul, P. J.; Noon, W. H.; Kittrell, C.; et al. Band Gap Fluorescence from Individual Single-Walled Carbon Nanotubes. *Science* **2002**, *297* (5581), 593–596.

(21)   Heller, D. A.; Baik, S.; Eurell, T. E.; Strano, M. S. Single-Walled Carbon Nanotube Spectroscopy in Live Cells: Towards Long-Term Labels and Optical Sensors. *Adv. Mater.* **2005**, *17* (23), 2793–2799.

(22)   HIRLEKAR, R.; YAMAGAR, M.; GARSE, H.; VIJ, M.; KADAM, V. CARBON NANOTUBES AND ITS APPLICATIONS: A REVIEW. *Asian J. Pharm. Clin. Res.* **2009**, No. 4, 11.

(23)   Jagota, A. Measurement of Electrostatic Properties of DNA-Carbon Nanotube Hybrids by Capillary Electrophoresis. *J. Phys. Chem. C* **2009**, *113* (31), 13616–13621.

(24)   Zheng, M.; Jagota, A.; Strano, M. S.; Santos, A. P.; Barone, P.; Chou, S. G.; Diner, B. A.; Dresselhaus, M. S.; McLean, R. S.; Onoa, G. B.; et al. Structure-Based Carbon Nanotube Sorting by Sequence-Dependent DNA Assembly. *Science* **2003**, *302* (5650), 1545–1548.

(25)   Lemoine; Kirkham, N.; Nicholas, R. *Progress in Pathology: - Google Books*; 2001.

(26) CSR. Lung and Bronchus Cancer - Cancer Stat Facts
https://seer.cancer.gov/statfacts/html/lungb.html (accessed Jul 6, 2018).

(27) Theme, L. A549 Cell Line Transfection, Protocol, Kits and Reagents - A549
Cell Line Transfection Protocol Reagent Method http://www.a549.com/
(accessed Jun 12, 2018).

(28) Lumen. Epithelial Tissue https://courses.lumenlearning.com/boundless-
ap/chapter/epithelial-tissue/ (accessed Jun 12, 2018).

(29) Gravely, M.; Roxbury, D. Comments about Size of A549 Cells, 2018.

(30) Smith, B. R.; Ghosn, E. E. B.; Rallapalli, H.; Prescher, J. A.; Larson, T.;
Herzenberg, L. A.; Gambhir, S. S. Selective Uptake of Single Walled Carbon
Nanotubes by Circulating Monocytes for Enhanced Tumour Delivery. *Nat.
Nanotechnol.* **2014**, *9* (6), 481–487.

(31) Liu, Z.; Cai, W.; He, L.; Nakayama, N.; Chen, K.; Sun, X.; Chen, X.; Dai, H. In
Vivo Biodistribution and Highly Efficient Tumour Targeting of Carbon
Nanotubes in Mice. *Nat. Nanotechnol.* **2007**, *2* (1), 47–52.

(32) Pantarotto, D.; Briand, J.-P.; Prato, M.; Bianco, A. Translocation of Bioactive
Peptides across Cell Membranes by Carbon Nanotubes. *Chem. Commun. Camb.
Engl.* **2004**, No. 1, 16–17.

(33) Pantarotto, D.; Singh, R.; McCarthy, D.; Erhardt, M.; Briand, J.-P.; Prato, M.;
Kostarelos, K.; Bianco, A. Functionalized Carbon Nanotubes for Plasmid DNA
Gene Delivery. *Angew. Chem. Int. Ed Engl.* **2004**, *43* (39), 5242–5246.

103

(34)   Kam, N. W. S.; Liu, Z.; Dai, H. Carbon Nanotubes as Intracellular Transporters for Proteins and DNA: An Investigation of the Uptake Mechanism and Pathway. *Angew. Chem. Int. Ed Engl.* **2006**, *45* (4), 577–581.

(35)   Shi Kam, N. W.; Jessop, T. C.; Wender, P. A.; Dai, H. Nanotube Molecular Transporters: Internalization of Carbon Nanotube−Protein Conjugates into Mammalian Cells. *J. Am. Chem. Soc.* **2004**, *126* (22), 6850–6851.

(36)   Chithrani, B. D.; Chan, W. C. W. Elucidating the Mechanism of Cellular Uptake and Removal of Protein-Coated Gold Nanoparticles of Different Sizes and Shapes - Nano Letters (ACS Publications) https://pubs.acs.org/doi/10.1021/nl070363y (accessed Jun 14, 2018).

(37)   Lee, P.-C.; Chiou, Y.-C.; Wong, J.-M.; Peng, C.-L.; Shieh, M.-J. Targeting Colorectal Cancer Cells with Single-Walled Carbon Nanotubes Conjugated to Anticancer Agent SN-38 and EGFR Antibody. *Biomaterials* **2013**, *34* (34), 8756–8765.

(38)   Kirchhausen, T. Three Ways to Make a Vesicle. *Nat. Rev. Mol. Cell Biol.* **2000**, *1* (3), 187–198.

(39)   Mukherjee, S.; Ghosh, R. N.; Maxfield, F. R. Endocytosis. *Physiol. Rev.* **1997**, *77* (3), 759–803.

(40)   Varkouhi, A. K.; Foillard, S.; Lammers, T.; Schiffelers, R. M.; Doris, E.; Hennink, W. E.; Storm, G. SiRNA Delivery with Functionalized Carbon Nanotubes. *Int. J. Pharm.* **2011**, *416* (2), 419–425.

(41)   Antonelli, A.; Serafini, S.; Menotta, M.; Sfara, C.; Pierigé, F.; Giorgi, L.;
       Ambrosi, G.; Rossi, L.; Magnani, M. Improved Cellular Uptake of
       Functionalized Single-Walled Carbon Nanotubes. *Nanotechnology* **2010**, *21*
       (42), 425101.

(42)   Marconi, U. M. B.; Puglisi, A.; Rondoni, L.; Vulpiani, A. Fluctuation-
       Dissipation: Response Theory in Statistical Physics. *Phys. Rep.* **2008**, *461* (4–
       6), 111–195.

(43)   Lesniak, A.; Salvati, A.; Santos-Martinez, M. J.; Radomski, M. W.; Dawson, K.
       A.; Åberg, C. Nanoparticle Adhesion to the Cell Membrane and Its Effect on
       Nanoparticle Uptake Efficiency. *J. Am. Chem. Soc.* **2013**, *135* (4), 1438–1444.

(44)   Di Silvio, D.; Maccarini, M.; Parker, R.; Mackie, A.; Fragneto, G.; Baldelli
       Bombelli, F. The Effect of the Protein Corona on the Interaction between
       Nanoparticles and Lipid Bilayers. *J. Colloid Interface Sci.* **2017**, *504*, 741–750.

(45)   Caracciolo, G.; Pozzi, D.; Capriotti, A. L.; Marianecci, C.; Carafa, M.;
       Marchini, C.; Montani, M.; Amici, A.; Amenitsch, H.; Digman, M. A.; et al.
       Factors Determining the Superior Performance of Lipid/DNA/Protammine
       Nanoparticles over Lipoplexes. *J. Med. Chem.* **2011**, *54* (12), 4160–4171.

(46)   Lundqvist, M.; Stigler, J.; Cedervall, T.; Berggård, T.; Flanagan, M. B.; Lynch,
       I.; Elia, G.; Dawson, K. The Evolution of the Protein Corona around
       Nanoparticles: A Test Study. *ACS Nano* **2011**, *5* (9), 7503–7509.

(47) Yang Sheng-Tao; Liu Ying; Wang Yan-Wen; Cao Aoneng. Biosafety and Bioapplication of Nanomaterials by Designing Protein–Nanoparticle Interactions. *Small* **2013**, *9* (9-10), 1635–1653.

(48) Jayme, D. W.; Epstein, D. A.; Conrad, D. R. Fetal Bovine Serum Alternatives | Nature. 1988.

(49) Kumar, N. Why should we add FBS to the serum free media? https://www.researchgate.net/post/Why_should_we_add_FBS_to_the_serum_free_media (accessed Jun 14, 2018).

(50) Arya, B. D.; Malik, N. Quantitative Estimation of Bovine Serum Albumin Protein Using UV -Visible Spectroscopy. **2015**, 4.

(51) Steinhardt, J.; Krijn, J.; Leidy, J. G. Differences between Bovine and Human Serum Albumins. Binding Isotherms, Optical Rotatory Dispersion, Viscosity, Hydrogen Ion Titration, and Fluorescence Effects. *Biochemistry (Mosc.)* **1971**, *10* (22), 4005–4015.

(52) Ge, C.; Du, J.; Zhao, L.; Wang, L.; Liu, Y.; Li, D.; Yang, Y.; Zhou, R.; Zhao, Y.; Chai, Z.; et al. Binding of Blood Proteins to Carbon Nanotubes Reduces Cytotoxicity. *Proc. Natl. Acad. Sci.* **2011**, *108* (41), 16968–16973.

(53) Chiu, J.-J.; Chien, S. Effects of Disturbed Flow on Vascular Endothelium: Pathophysiological Basis and Clinical Perspectives. *Physiol. Rev.* **2011**, *91* (1).

(54) Turitto, V. T. Blood Viscosity, Mass Transport, and Thrombogenesis. *Prog. Hemost. Thromb.* **1982**, *6*, 139–177.

(55) Pedersen, J. A.; Boschetti, F.; Swartz, M. A. Effects of Extracellular Fiber
Architecture on Cell Membrane Shear Stress in a 3D Fibrous Matrix. *J. Biomech.* **2007**, *40* (7), 1484–1492.

(56) Tarbell, J. M.; Shi, Z.-D. Effect of the Glycocalyx Layer on Transmission of
Interstitial Flow Shear Stress to Embedded Cells. *Biomech. Model. Mechanobiol.* **2013**, *12* (1), 111–121.

(57) Cornish, R. J. Flow in a Pipe of Rectangular Cross-Section. *Proc R Soc Lond A* **1928**, *120* (786), 691–700.

(58) IBIDI GmbH. Shear Stress and Shear Rates for ibidi μ-Slides - Based on
Numerical Calculations https://ibidi.com/channel-slides/50--slide-i-luer.html
(accessed Apr 29, 2018).

(59) Brody, J. P.; Yager, P.; Goldstein, R. E.; Austin, R. H. Biotechnology at Low
Reynolds Numbers. *Biophys. J.* **1996**, *71* (6), 3430–3441.

(60) Stone, H. A.; Stroock, A. D.; Ajdari, A. Engineering Flows in Small Devices:
Microfluidics Toward a Lab-on-a-Chip. *Annu. Rev. Fluid Mech.* **2004**, *36* (1), 381–411.

(61) Terhal, B. M.; Horodecki, P. Schmidt Number for Density Matrices. *Phys. Rev. A* **2000**, *61* (4), 040301.

(62) Hagen, N.; Michael W., K. SPIE | Optical Engineering | Review of snapshot
spectral imaging technologies

https://web.archive.org/web/20150920195938/http://opticalengineering.spiedigitallibrary.org/article.aspx?articleid=1743003 (accessed Jun 5, 2018).

(63) Veys, C.; Hibbert, J.; Davis, P.; Grieve, B. An Ultra-Low-Cost Active Multispectral Crop Diagnostics Device; IEEE, 2017; pp 1–3.

(64) Kruss, S.; Landry, M. P.; Vander Ende, E.; Lima, B. M. A.; Reuel, N. F.; Zhang, J.; Nelson, J.; Mu, B.; Hilmer, A.; Strano, M. Neurotransmitter Detection Using Corona Phase Molecular Recognition on Fluorescent Single-Walled Carbon Nanotube Sensors. *J. Am. Chem. Soc.* **2014**, *136* (2), 713–724.

(65) Heller, D. A.; Jin, H.; Martinez, B. M.; Patel, D.; Miller, B. M.; Yeung, T.-K.; Jena, P. V.; Höbartner, C.; Ha, T.; Silverman, S. K.; et al. Multimodal Optical Sensing and Analyte Specificity Using Single-Walled Carbon Nanotubes. *Nat. Nanotechnol.* **2009**, *4* (2), 114–120.

(66) Ahn, J.-H.; Kim, J.-H.; Reuel, N. F.; Barone, P. W.; Boghossian, A. A.; Zhang, J.; Yoon, H.; Chang, A. C.; Hilmer, A. J.; Strano, M. S. Label-Free, Single Protein Detection on a near-Infrared Fluorescent Single-Walled Carbon Nanotube/Protein Microarray Fabricated by Cell-Free Synthesis. *Nano Lett.* **2011**, *11* (7), 2743–2752.

(67) Roxbury, D.; Jena, P. V.; Williams, R. M.; Enyedi, B.; Niethammer, P.; Marcet, S.; Verhaegen, M.; Blais-Ouellette, S.; Heller, D. A. Hyperspectral Microscopy of Near-Infrared Fluorescence Enables 17-Chirality Carbon Nanotube Imaging. *Sci. Rep.* **2015**, *5*, 14167.

(68) Broda, E.; Mickler, F. M.; Lächelt, U.; Morys, S.; Wagner, E.; Bräuchle, C. Assessing Potential Peptide Targeting Ligands by Quantification of Cellular Adhesion of Model Nanoparticles under Flow Conditions. *J. Controlled Release* **2015**, *213*, 79–85.

(69) Farokhzad, O. C.; Khademhosseini, A.; Jon, S.; Hermmann, A.; Cheng, J.; Chin, C.; Kiselyuk, A.; Teply, B.; Eng, G.; Langer, R. Microfluidic System for Studying the Interaction of Nanoparticles and Microparticles with Cells. *Anal. Chem.* **2005**, *77* (17), 5453–5459.

(70) IBIDI GmbH. µ-Slides and µ-Dishes; Instructions and FAQ; ibidi https://ibidi.com/content/28-m-slides-and-m-dishes#c377; https://ibidi.com/img/cms/products/labware/channel_slides/S_801XX_Slide_IL uer/IN_801XX_I_Luer.pdf (accessed Jun 4, 2018).

(71) Funk, S. D.; Yurdagul, A.; Green, J. M.; Jhaveri, K. A.; Schwartz, M. A.; Orr, A. W. Matrix-Specific Protein Kinase A Signaling Regulates P21 Activated Kinase Activation by Flow in Endothelial Cells. *Circ. Res.* **2010**, *106* (8), 1394–1403.

(72) Schmid-Schönbein, H.; Rieger, H.; Fischer, T. Blood Fluidity as a Consequence of Red Cell Fluidity: Flow Properties of Blood and Flow Behavior of Blood in Vascular Diseases. *Angiology* **1980**, *31* (5), 301–319.

(73) Nerem, R. M.; Alexander, R. W.; Chappell, D. C.; Medford, R. M.; Varner, S. E.; Taylor, W. R. The Study of the Influence of Flow on Vascular Endothelial Biology. *Am. J. Med. Sci.* **1998**, *316* (3), 169–175.

(74)   Bäcker, V. Workshop : Image Processing and Analysis with ImageJ and MRI Ce. **2008**, 75.

(75)   Mody, N. A.; King, M. R. Influence of Brownian Motion on Blood Platelet Flow Behavior and Adhesive Dynamics near a Planar Wall. *Langmuir ACS J. Surf. Colloids* **2007**, *23* (11), 6321–6328.

(76)   Guermonprez, C.; Michelin, S.; Baroud, C. N. Flow Distribution in Parallel Microfluidic Networks and Its Effect on Concentration Gradient. *Biomicrofluidics* **2015**, *9* (5).

(77)   Lane, W. O.; Jantzen, A. E.; Carlon, T. A.; Jamiolkowski, R. M.; Grenet, J. E.; Ley, M. M.; Haseltine, J. M.; Galinat, L. J.; Lin, F.-H.; Allen, J. D.; et al. Parallel-Plate Flow Chamber and Continuous Flow Circuit to Evaluate Endothelial Progenitor Cells under Laminar Flow Shear Stress. *J. Vis. Exp. JoVE* **2012**, No. 59.

(78)   Waluch, V.; Bradley, W. G. NMR Even Echo Rephasing in Slow Laminar Flow. *J. Comput. Assist. Tomogr.* **1984**, *8* (4), 594–598.

(79)   Keltner, J. R.; Roos, M. S.; Brakeman, P. R.; Budinger, T. F. Magnetohydrodynamics of Blood Flow. *Magn. Reson. Med.* **2005**, *16* (1), 139–149.

(80)   Roxbury, D. Nanosensor Device May Help Watch for Cancer From the Inside https://www.cancer.org/latest-news/nanosensor-device-may-help-watch-for-cancer-from-the-inside.html (accessed Jun 14, 2018).

(81)   Labrecque, S.; Sylvestre, J.-P.; Marcet, S.; Mangiarini, F.; Bourgoin, B.;
        Verhaegen, M.; Blais-Ouellette, S.; Koninck, P. D. Hyperspectral Multiplex
        Single-Particle Tracking of Different Receptor Subtypes Labeled with Quantum
        Dots in Live Neurons. *J. Biomed. Opt.* **2016**, *21* (4), 046008.

(82)   Roxbury Lab. Lab Facilities https://web.uri.edu/nanobiolab/facilities/ (accessed
        Jun 14, 2018).

(83)   Lindl, T. Components of Fetal Bovine Serum from Lindl, T. (2002). In *Zell-
        und Gewebekultur*; 5th edition; Spektrum Akademischer Verlag, Heidelberg,
        2002.

(84)   Gstraunthaler, G. Alternatives to the Use of Fetal Bovine Serum: Serum-Free
        Cell Culture. *Pharmacol. Ther.* **1992**, *53* (3), 355–374.

(85)   Price, P. J.; Gregory, E. A. Relationship between in Vitro Growth Promotion
        and Biophysical and Biochemical Properties of the Serum Supplement. *In Vitro*
        1982, *18* (6), 576–584.

(86)   Ge, S.; Kojio, K.; Takahara, A.; Kajiyama, T. Bovine Serum Albumin
        Adsorption onto Immobilized Organotrichlorosilane Surface: Influence of the
        Phase Separation on Protein Adsorption Patterns. *J. Biomater. Sci. Polym. Ed.*
        1998, *9* (2), 131–150.

(87)   McLachlan, A. D.; Walker, J. E. Evolution of Serum Albumin. *J. Mol. Biol.*
        1977, *112* (4), 543–558.

(88) Wright, A. K.; Thompson, M. R. Hydrodynamic Structure of Bovine Serum Albumin Determined by Transient Electric Birefringence. *Biophys. J.* **1975**, *15* (2), 137–141.

(89) Putnam, F. W. *The Plasma Proteins*; 2nd Edition; 1975.

(90) Sigma-Aldrich. Albumin from Bovine Serum. July 5, 2013.

(91) Axelsson, I. Characterization of Proteins and Other Macromolecules by Agarose Gel Chromatography. *J. Chromatogr. A* **1978**, *152* (1), 21–32.

(92) SigmaAldrich. L-Glutamine in Cell Culture https://www.sigmaaldrich.com/life-science/cell-culture/learning-center/media-expert/glutamine.html (accessed Jun 7, 2018).

(93) Good, N. E.; Winget, G. D.; Winter, W.; Connolly, T. N.; Izawa, S.; Singh, R. M. M. Hydrogen Ion Buffers for Biological Research*. *Biochemistry (Mosc.)* **1966**, *5* (2), 467–477.

(94) ThermoFisher. HEPES - US https://www.thermofisher.com/us/en/home/life-science/cell-culture/mammalian-cell-culture/reagents/hepes.html (accessed Jun 7, 2018).